PHYSICAL REVIEW B VOLUME 54, NUMBER 16 15 OCTOBER 1996-II

Dynamical response of double parabolically graded quantum wells

L. Wendler
Anna-Siemsen-Straße 66, D-07745 Jena, Germany

T. Kraft
Fachbereich Physik, Martin-Luther-Universität Halle, Friedemann-Bach-Platz 6, D-06108 Halle, Germany

(Received 11 April 1996)

The collective charge-density excitations, the intra- and intersubband plasmons, and their manifestation in far-infrared transmission spectroscopy are studied for coupled quantum wells. We calculate self-consistently the ground state in the Hartree approximation and the density response in the random-phase approximation. We investigate the plasmons in symmetric coupled quantum wells in dependence on the coupling between the two wells and study the effects of deviation from the spatial symmetry. It is shown that the intersubband coupling forms a hybrid-type mode spectrum. The strong hybridization of the collective intrasubband motion with the lowest-frequency intersubband transition presses one branch in the single-particle intrasubband continuum and the higher-frequency intersubband modes form doublets. The optical transmission spectra of these samples with a grating coupler above the electron system show a strong exchange of oscillator strength between the modes. [S0163-1829(96)08735-8]

I. INTRODUCTION

The quasi-two-dimensional electron gas (Q2DEG) has received an extraordinary amount of attention from semiconductor physics for many years.[1] This is somewhat because of its technological importance in microelectronic and optoelectronic devices but also due to the fact that the study of the Q2DEG has revealed remarkable phenomena associated with electron-electron interactions under reduced dimensions. The excitation spectrum of the electron gas gives important insights in the electron-electron interaction mechanisms and thus the need to understand the fundamental interaction processes stimulates theoretical and experimental research of the collective excitations of the Q2DEG. Far-infrared (FIR) transmission spectroscopy and inelastic light scattering experiments have both yielded detailed informations about the collective charge-density excitations (CDE's), the plasmons, which exist through direct and image parts of the Coulomb interaction. In addition, collective spin-density excitations (SDE's), which are manifestations of the exchange and correlation parts of the Coulomb interaction in Q2DEG's and single-particle excitations (SPE's; electron-hole pair excitations), are observable in inelastic light scattering. The splitting between the different excitations is a measure of the different electron-electron interaction mechanisms.

The most important collective excitation of the Q2DEG is the plasmon. Q2D plasmons have been investigated theoretically, e.g., Refs. 1–10 and experimentally, e.g., Refs. 11–18. Caused by the size quantization, the collective excitation spectrum becomes split in intrasubband plasmons, connected with electron motion within one subband and intersubband plasmons, connected with electron transitions between two different subbands. For usual electron densities the Q2D intersubband plasmons have frequencies above the corresponding single-particle transition frequencies. This frequency shift is caused by many-particle effects and consists of two parts. The first part is the so-called depolarization shift, is always positive, and is caused by resonance screening and thus described within the framework of the random-phase approximation (RPA). The second part, which is beyond the RPA, is the so-called excitonic shift, which is a negative contribution to the frequency shift of an intersubband plasmon and caused by exchange-correlation effects. Decreasing the density of the electron gas, it becomes possible that the excitonic shift becomes larger in magnitude than the depolarization shift and thus, the intersubband plasmon has a frequency below the corresponding subband separation frequency.[19,20]

A peculiarity arises if the bare confining potential has a perfect parabolic shape. In this case, the generalized Kohn's theorem[21,22] predicts that in a FIR experiment, the Q2DEG absorbs radiation only at the bare harmonic oscillator frequency, which is the unrenormalized subband separation frequency, independent of the electron-electron interaction and the number of electrons in the parabolic quantum well (PQW). This collective intersubband resonance (collective intersubband transition, dimensional resonance) is called Kohn's mode (or sometimes fundamental mode) and corresponds to the center-of-mass motion of all confined electrons. From the point of view of many-particle physics the generalized Kohn's theorem predicts the exact cancellation of the renormalization of the subband separation frequency (self-energy effect) with the depolarization and the excitonic shift of this mode. Deviations from the perfect parabolicity will break Kohn's theorem with the result that the frequency of Kohn's mode now becomes density dependent and higher intersubband resonances become visible.[23] For this reason, optical measurements are useful in characterizing the spatial shape of the confining potential. While the collective excitations of single quantum wells (SQW's) have been extensively studied, there have been only a few theoretical studies of double quantum wells (DQW's).[24,25] But in recently performed experiments on DQW's interesting physical effects were observed. Decca *et al.*[26] showed that the excitonic shift to the intersubband SDE vanishes in a DQW in the high-density limit, i.e., the SDE's and SPE's cannot be distinguished in inelastic light scattering spectra. Further, Hartung *et al.*[27] observed in FIR transmission spectra of DQW's a strong exchange of oscillator strength between two collective intersubband resonances.

The aim of the present paper is to investigate the Q2D plasmons and their optical manifestation in double parabolically graded quantum wells (DPQW's), i.e., two coupled quantum wells, with parabolic shape, in dependence on the coupling of the two wells and study the effects when the two wells become asymmetric coupled. The work is performed by self-consistent calculations of the ground state in the Hartree approximation and the density response in the framework of the random-phase approximation. In Sec. II we calculate the ground-state properties of the Q2DEG in DPQW's and in Sec. III we develop the method to calculate the density response of the electron system. In Sec. IV we investigate the dispersion relation of the Q2D plasmons for different DPQW's, i.e., we study the influence of the coupling of the two wells, deviations from the parabolic shape and spatial asymmetry of the confining potential. In Sec. V we calculate the optical transmission spectra of semiconductor samples containing the above electron systems and a grating coupler on top to couple the FIR radiation to the collective excitations of the Q2DEG. Finally, in Sec. VI we summarize our results.

II. GROUND STATE

A. General

We consider two different quantum-well-structures: (i) a single truncated PQW (SPQW) and (ii) two coupled truncated PQW's, i.e., forming the DPQW with conduction-band edges schematically illustrated in Fig. 1. These wells have a finite width w, a depth V_1 of the parabola, and an additionally barrier of height V_2 due to the conduction-band edge discontinuity at the heterointerface between the $\mathrm{Ga}_{1-y}\mathrm{Al}_y\mathrm{As}$ QW and the $\mathrm{Ga}_{1-x}\mathrm{Al}_x\mathrm{As}$ barrier $(y<x)$, i.e., the conduction-band edge acts as the bare confining potential $V_0(z)=E_c(z)$. Such structures may be realized by molecular beam epitaxy by appropriately grading the aluminium content of the $\mathrm{Ga}_{1-y}\mathrm{Al}_y\mathrm{As}$ layer during growth. To describe the electrons in the host semiconductor, we use the effective-mass approximation assuming a uniform effective mass m_e. We also take the static dielectric constant ε_s to be uniform across the sample, i.e., neglect image effects. In actual GaAs-$\mathrm{Ga}_{1-x}\mathrm{Al}_x\mathrm{As}$ heterostructures these inhomogeneity effects have only a small influence on the electronic ground-state properties of the system.[28] Electrons from the donors in the adjacent $\mathrm{Ga}_{1-x}\mathrm{Al}_x\mathrm{As}$ barriers enter the QW and form the Q2DEG in the SPQW and the DPQW. The interacting electrons of the Q2DEG will screen the bare potential, so that the so-called effective potential (self-consistent potential or total potential) $V_{eff}(z)$ arises, which can be separated into the bare potential $V_0(z)$ and the Hartree potential $V_H(z)=-e\Phi(z)$, due to the electrostatic potential of the mobile electrons of the Q2DEG and the spatial fixed ionized donors, and the exchange-correlation potential $V_{xc}(z)$. The last one we neglect in this paper. This is possible for the usual electron densities. Within the approximations made above the one-electron motion is given by the effective Schrödinger equation

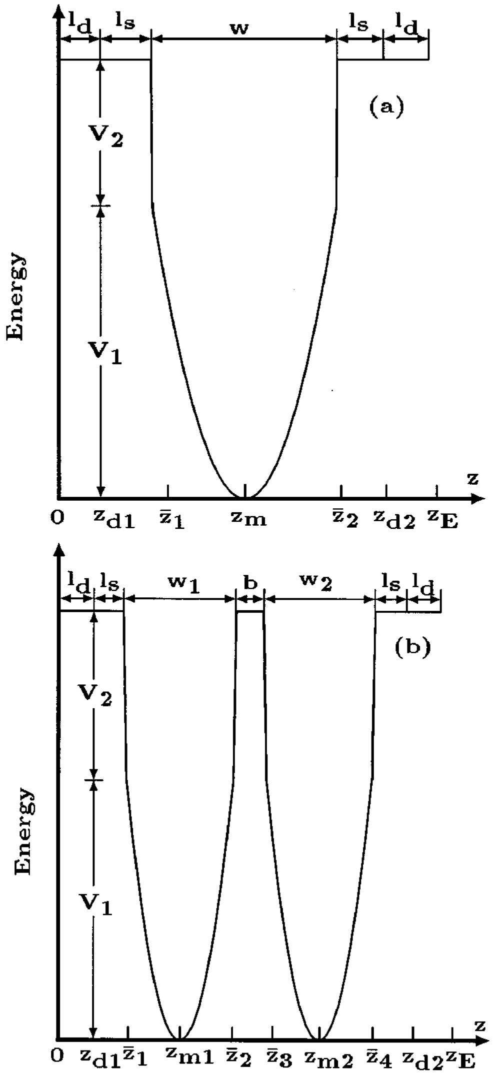

FIG. 1. Schematic arrangement of the bare potential of a SPQW (a) and of a DPQW (b).

$$\left(-\frac{\hbar^2}{2m_e}\nabla^2+V_{eff}(z)\right)\Psi_{K\mathbf{k}_\parallel}(\mathbf{x})=\mathcal{E}_K(\mathbf{k}_\parallel)\Psi_{K\mathbf{k}_\parallel}(\mathbf{x}). \tag{1}$$

With respect to the translational symmetry in the x-y plane the single-particle wave function $\Psi_{K\mathbf{k}_\parallel}(\mathbf{x})$ is

$$\langle\mathbf{x}|K\mathbf{k}_\parallel\rangle=\Psi_{K\mathbf{k}_\parallel}(\mathbf{x})=\frac{1}{\sqrt{A}}e^{i\mathbf{k}_\parallel\cdot\mathbf{x}_\parallel}\varphi_K(z) \tag{2}$$

and the associated eigenvalues, the Q2D subbands, read

$$\mathcal{E}_K(\mathbf{k}_\parallel)=\mathcal{E}_K+\frac{\hbar^2k_\parallel^2}{2m_e},\quad K=0,1,2,\ldots. \tag{3}$$

Herein, $\mathbf{x}_{\parallel}=(x,y)$ and $\mathbf{k}_{\parallel}=(k_x,k_y)$ are the 2D position and wave vector in the x-y plane, respectively, $k_{\parallel}=|\mathbf{k}_{\parallel}|$ and A is the unit area in this plane assuming Born–von Kármán boundary conditions. In the following, we suppose spin degeneracy and omit the spin index. The spin summation is assumed to be included when necessary without any explicit indication. The bottoms of the subbands $\mathcal{E}_K$ and the envelope wave function are obtained from the one-dimensional Schrödinger equation

$$\left(-\frac{\hbar^2}{2m_e}\frac{d^2}{dz^2}+V_{eff}(z)\right)\varphi_K(z)=\mathcal{E}_K\varphi_K(z), \tag{4}$$

where the envelope wave functions are orthonormalized according to

$$\int_{-\infty}^{\infty} dz\,\varphi_K^*(z)\varphi_{K'}(z)=\delta_{KK'} \tag{5}$$

and the effective potential is $V_{eff}(z)=V_0(z)+V_H(z)$. The bare potential $V_0(z)$, resulting from the tailoring of the conduction-band edge, depends on the Al concentration at the position z, and the Hartree potential results from the electrostatic interaction of the electrons with themselves and from the ionized impurity charges, and thus, is given by Poisson's equation

$$\frac{d^2}{dz^2}V_H(z)=-\frac{e^2}{\varepsilon_0\varepsilon_s}[n_0(z)-N_D^+(z)]. \tag{6}$$

In this equation the electron charge is $-e$, ε_0 is the permittivity in vacuum and the ground-state (equilibrium) electron number density at $T=0$ K is given by

$$n_0(z)=\sum_K n_0^{(K)}(z), \tag{7}$$

$$n_0^{(K)}(z)=\frac{m_e}{\pi\hbar^2}|\varphi_K(z)|^2(E_F-\mathcal{E}_K)\Theta(E_F-\mathcal{E}_K), \tag{8}$$

where $n_0^{(K)}(z)$ is the contribution of the Kth subband to the electron density profile, $\Theta(x)$ is the Heaviside unit step function with $\Theta(x)=1$ for $x>0$ and $\Theta(x)=0$ for $x<0$, and the Fermi energy E_F is determined from the electron number density (number of electrons per unit area, sheet carrier concentration)

$$n_{2DEG}=\sum_K N_K, \tag{9}$$

$$N_K=\frac{m_e}{\pi\hbar^2}(E_F-\mathcal{E}_K)\Theta(E_F-\mathcal{E}_K), \tag{10}$$

where N_K is the sheet carrier concentration of the Kth subband. The Fermi wave vectors of the different subbands are given by

$$k_F^{(K)}=\begin{cases}\sqrt{2m_e(E_F-\mathcal{E}_K)/\hbar^2} & \text{if } E_F>\mathcal{E}_K\\ 0 & \text{if } E_F\leqslant\mathcal{E}_K\end{cases} \tag{11}$$

and the corresponding Fermi velocities are $v_F^{(K)}=\hbar k_F^{(K)}/m_e$.

The self-consistent solution of Eqs. (4)–(10) gives the subband energies, the charge-density profile, the Fermi energy, and the effective potential. To solve Poisson's equation we have to specify our model. We assume that the QW's as well as the barrier of thickness b between the two wells and the spacer layers of finite thickness l_s are undoped. The Ga$_{1-x}$Al$_x$As layers embedding the SPQW or the DPQW are assumed to be uniformly doped with donors. The donor levels are all supposed to lie at an energy E_b below the conduction band. The donors are completely ionized in the depletion regions of thickness l_d to the right and left from the QW's. Because the donors outside the depletion layers are neutral, the Fermi level of the whole heterojunction can therefore be identified with the donor energy level at $z\rightarrow 0$ and $z\rightarrow z_E$ to the left and right of the depletion layers. If we put $E_F=0$ as reference level, we have $V_{eff}(0)=V_{eff}(z_E)=E_b$, acting as boundary condition in solving Poisson's equation. The charge density is now equal to

$$N_D^+(z)=\begin{cases} eN_D^+, & 0<z<z_{d1}\\ 0, & z_{d1}<z<z_{d2}\\ eN_D^+, & z_{d2}<z<z_E\end{cases} \tag{12}$$

where (i) for the SPQW structure we have $z_{d1}=l_d$, $z_{d2}=l_d+l_s+w+l_s$, and $z_E=z_{d2}+l_d$ and (ii) for the DPQW structures we have $z_{d1}=l_d$, $z_{d2}=l_d+l_s+w_1+b+w_2+l_s$, and $z_E=z_{d2}+l_d$.

Integrating Eq. (6) twice from $z=0$ to $z=z_E$, using the continuity of $V_H(z)$ and $d/dz\,V_H(z)$ at the boundaries of the sample, $n_0(z)\rightarrow 0$ for $z\rightarrow 0$ and $z\rightarrow z_E$ and the boundary conditions $V_{eff}(0)=V_{eff}(z_E)=E_b$, we obtain

$$V_H(z)=-\frac{e^2}{\varepsilon_0\varepsilon_s}\int_0^z dz'(z-z')n_0(z')+eN_D^+\begin{cases}\frac{1}{2}z^2, & 0\leqslant z\leqslant z_{d1}\\ \frac{1}{2}l_d^2+(z-z_{d1})l_d, & z_{d1}\leqslant z\leqslant z_{d2}\\ \frac{1}{2}l_d^2+(z_{d2}-z_{d1})l_d+\frac{1}{2}(z-z_{d2})^2+(z-z_{d2})l_d, & z_{d2}\leqslant z\leqslant z_E.\end{cases} \tag{13}$$

The charge neutrality of the sample $\int_0^{z_E}dz[n_0(z)-N_D^+(z)]=0$, gives $n_{2DEG}=2l_dN_D^+$.

For the bare potential we use the following model potentials, depicted in Fig. 1: (i) SPQW,

$$V_0(z)=\begin{cases} V_1+V_2, & 0<z<\overline{z_1}\\ \frac{1}{2}\,m_e\Omega^2(z-z_m)^2, & \overline{z_1}<z<\overline{z_2}\\ V_1+V_2, & \overline{z_2}<z,\end{cases} \tag{14}$$

where $\overline{z_1}=l_d+l_s$, $\overline{z_2}=\overline{z_1}+w$ and $z_m=\overline{z_1}+w/2$; (ii) DPQW

$$V_0(z)=\begin{cases} V_1+V_2, & 0<z<\overline{z_1}\\ \frac{1}{2}\,m_e\Omega_1^2(z-z_{m1})^2, & \overline{z_1}<z<\overline{z_2}\\ V_1+V_2, & \overline{z_2}<z<\overline{z_3}\\ \frac{1}{2}\,m_e\Omega_2^2(z-z_{m2})^2, & \overline{z_3}<z<\overline{z_4}\\ V_1+V_2, & \overline{z_4}<z,\end{cases} \tag{15}$$

where $\overline{z_1}=l_d+l_s$, $\overline{z_2}=\overline{z_1}+w_1$, $\overline{z_3}=\overline{z_2}+b$, and $\overline{z_4}=\overline{z_3}+w_2$. The variation of the different parameter allows to describe with Eq. (15) different types of DPQW's.

Now we have to solve the Schrödinger equation with the effective potential self-consistently. Such a fully self-consistent procedure would give n_{2DEG} and the depletion length l_d as results,[29] which may be different on the right- and left-hand side of the QW. To simplify the numerical handling, without restrictions for the generality of the results, we assume that the depletion length l_d is considered as an input parameter and identical on both sides. This simplification gives quite satisfactory results because our goals are the dynamical properties of these systems and not high accuracy ''first'' principle model calculations of the subband energies of given systems.

B. Numerical results

In our calculations we use the following set of parameters: $\varepsilon_s=12.87$, $m_e=0.06624m_0$ typical for GaAs, where m_0 is the bare electron mass. We assume that the parabolic potentials are truncated at $V_1=150$ meV at $\overline{z_1}$ and $\overline{z_2}$ in the case of the SPQW and at $\overline{z_1}$ and $\overline{z_4}$ in the case of the DPQW. Further, the barrier height of the square well potential is $V_2=75$ meV at these positions. For the thickness of the spacer layers we assume $l_s=5$ nm and the thickness of the depletion layers is assumed to be $l_d=5$ nm. Thus, the confining frequency Ω of the parabolic potential of a SPQW is related to the width w via $\Omega=[8V_1/(m_ew^2)]^{1/2}$ and we use $\hbar\Omega=29.22$ meV.

Further, we investigate three different DPQW's: the symmetric DPQW, the symmetric truncated DPQW, and the asymmetric truncated DPQW. For the symmetric DPQW each PQW is symmetric with respect to z_{m1} and z_{m2}, respectively, and the two PQW's are identical: $w=w_1=w_2=40$ nm and $\Omega=\Omega_1=\Omega_2=[8V_1/(m_ew^2)]^{1/2}$ and we use $\hbar\Omega=29.22$ meV. Then, $z_{m1}=\overline{z_1}+w/2$, $z_{m2}=\overline{z_3}+w/2$, and $V_0(\overline{z_1})=V_0(\overline{z_2})=V_0(\overline{z_3})=V_0(\overline{z_4})=V_1$ is valid. We investigate the symmetric DPQW for different barrier thicknesses b in the range from $b=1$ nm to $b=10$ nm. The single PQW's of the symmetric truncated DPQW are not symmetric with respect to z_{m1} and z_{m2}, respectively. They are truncated at $\overline{z_1}$, $\overline{z_2}$, $\overline{z_3}$, and $\overline{z_4}$, so that $V_0(\overline{z_1})=V_0(\overline{z_4})=V_1$, but $V_0(\overline{z_2})=V_0(\overline{z_3})\neq V_1$ is valid. We consider two PQW's with the same curvature $\Omega=\Omega_1=\Omega_2=[8V_1/(m_e\overline{w}^2)]^{1/2}$ and use $\hbar\Omega=29.22$ meV. Here, $\overline{w}=40$ nm is the width of the corresponding single symmetric PQW which determines the positions $z_{m1}=\overline{z_1}+\overline{w}/2$ and $z_{m2}=\overline{z_4}-\overline{w}/2$. Further, we use $w=w_1=w_2=30$ nm$\neq\overline{w}$ from which together with l_s, l_d, and b the positions $\overline{z_1}$, $\overline{z_2}$, $\overline{z_3}$, and $\overline{z_4}$ are fixed. For the barrier thickness we choose $b=1$ nm. For the asymmetric truncated DPQW the single PQW's are not symmetric with respect to z_{m1} and z_{m2}, respectively, and further they are truncated at $\overline{z_1}$, $\overline{z_2}$, $\overline{z_3}$, and $\overline{z_4}$, so that $V_0(\overline{z_1})=V_0(\overline{z_4})=V_1$, but $V_0(\overline{z_2})\neq V_0(\overline{z_3})\neq V_1$ is valid. The curvatures of the single PQW's of the asymmetric truncated DPQW are identical, as in the case of the symmetric truncated DPQW, but the widths of the single PQW's are different: $w_1=32$ nm $\neq w_2=30$ nm. Thus, we have in this case $z_{m1}=\overline{z_1}+\overline{w}/2$ and $z_{m2}=\overline{z_4}-\overline{w}/2$ and we choose $b=1$ nm.

The Schrödinger equation is solved numerically with the help of the difference method. Starting from an arbitrary potential (here, we use the bare potential) we solve the Schrödinger equation, i.e., find eigenfunctions and eigenenergies, determine the Fermi energy and the sheet carrier concentrations of the subbands and then obtain the Hartree potential. With this solution we solve the Schrödinger equation again and obtain a new solution. We repeat this cycle until convergence, i.e., self-consistency, is reached. We test the convergence of the procedure by the subband energies and demand $|(\mathcal{E}_K^{(i+1)}-\mathcal{E}_K^{(i)})/\mathcal{E}_K^{(i)}|\leqslant 10^{-5}$ meV, where i is the number of the iteration.

1. Single parabolic quantum wells

In Fig. 2 we show the bare potential, the effective potential, and the five lowest subband energies measured from the Fermi energy ($E_F=0$), for two different electron densities. It is seen from Fig. 2 that with increasing density the bottom of the PQW becomes flatter and the subband separation decreases. Thus, the contribution of the Hartree potential to $V_{eff}(z)$ increases with increasing electron concentration: $V_{eff}(z)$ deforms in $\overline{z_1}<z<\overline{z_2}$ from a nearly parabolic shape to a more and more rectangular shape and bends $V_{eff}(z)$ in the regions $z<\overline{z_1}$ and $z>\overline{z_2}$. The five lowest subband energies $\mathcal{E}_K$ are plotted versus the electron density in Fig. 3. It is seen that with increasing density of the Q2DEG in the SPQW the subband separation frequency $\Omega_{KK'}=(\mathcal{E}_K-\mathcal{E}_{K'})/\hbar$ decreases nearly linearly: $\Omega_{10}=4.46\times10^{13}$ s^{-1} for $n_{2DEG}=1\times10^{7}$ cm^{-2}, $\Omega_{10}=4.19\times10^{13}$ s^{-1} for $n_{2DEG}=1\times10^{11}$ cm^{-2} and $\Omega_{10}=3.14\times10^{13}$ s^{-1} for $n_{2DEG}=5\times10^{11}$ cm^{-2}. Thus, at low electron concentrations the lowest subband separation frequency is nearly equal to the bare harmonic oscillator frequency $\Omega_{10}=\Omega$ of an effective parabolic potential $V_{eff}(z)=(m_e\Omega^2/2)z^2$. Deviations result from the hard walls and the finite height of the barriers. The electron density profile calculated from Eq. (7) is depicted in Fig. 4. Because the SPQW is mirror symmetric at $z=z_m$ there are two different sets of envelope wave functions $\varphi_K(z)$: even parity states (symmetric wave functions) $\varphi_0(z)$, $\varphi_2(z)$, $\varphi_4(z)$, . . . and odd parity states (antisymmetric wave function) $\varphi_1(z)$, $\varphi_3(z)$, $\varphi_5(z)$, ...

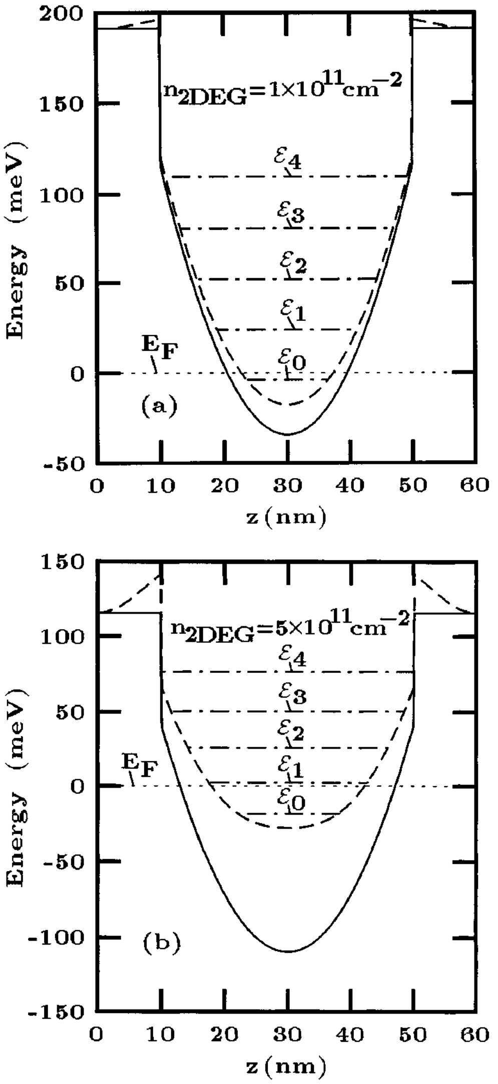

FIG. 2. Bare potential (solid line), effective potential (dashed lined), subband energies (dashed-dotted line), and Fermi energy (dotted line) of a SPQW for two different electron number densities: (a) $n_{2DEG}=1\times10^{11}$ cm^{-2}, (b) $n_{2DEG}=5\times10^{11}$ cm^{-2}. The Fermi energy (dotted line) is chosen to be $E_F=0$.

2. *Double parabolic quantum wells*

The corresponding results are plotted for the three different DPQW's in Figs. 5, 7, and 8. Because the electrons can tunnel through the barrier between the two PQW's (''coupled PQW's'') the degeneracy of the energy levels becomes lifted and thus, the subbands of the DPQW's arise as doublets. First, we consider the symmetric DPQW. The bare potential, the effective potential and the six lowest subband energies measured from the Fermi energy, are plotted in Fig. 5(a) for $n_{2DEG}=1\times10^{11}$ cm^{-2}. The splitting of these subbands, $\mathcal{E}_0$ and $\mathcal{E}_1$, $\mathcal{E}_2$ and $\mathcal{E}_3$, $\mathcal{E}_4$ and $\mathcal{E}_5$, is very small and not to be drawn in Fig. 5(a). In Fig. 6 the splitting of the doublet $\mathcal{E}_1-\mathcal{E}_0$ is plotted versus the barrier thickness b for three different densities of the Q2DEG. It is seen that the level splitting decreases with increasing barrier thickness and with increasing electron density. The second dependence is a result of the increasing Coulomb repulsion of the electrons in the two QW's with increasing number of electrons. The six lowest subband energies $\mathcal{E}_K$ are plotted versus the electron density in Fig. 7(a). It is seen that for the chosen density range two subbands, $\mathcal{E}_0$ and $\mathcal{E}_1$ (the lowest doublet), are occupied. From the density profile $n_0(z)$, plotted in Fig. 8(a) for two different sheet carrier concentrations n_{2DEG}, it becomes obvious that the relative thick barrier between the two QW's more or less separates the two electron systems.

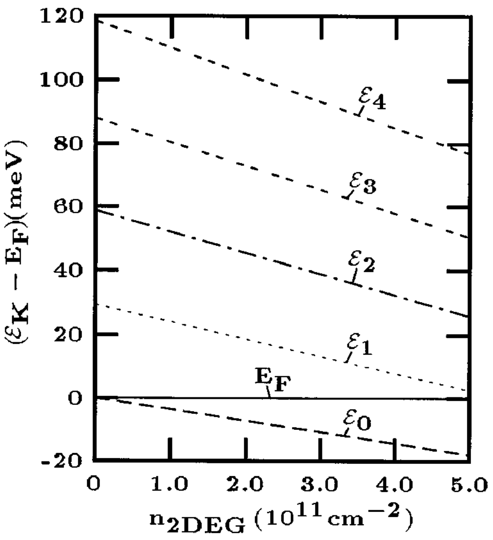

FIG. 3. Subband energies of the SPQW in dependence on the electron number density. The Fermi energy (solid line) is chosen to be $E_F=0$.

For the symmetric truncated DPQW, which we consider now, the barrier thickness between the two QW's is much smaller and thus, the separation of the doublets increases. This is seen from Fig. 5(b), where we have plotted the bare and effective potential and the six lowest subband energies. It becomes obvious that the splitting of the doublets is larger for the higher subbands as for the lower subbands. Again this

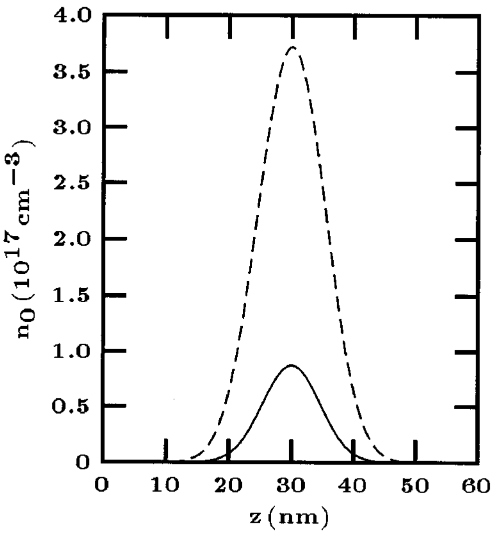

FIG. 4. Electron density profiles of the SPQW for $n_{2DEG}=1\times10^{11}$ cm^{-2} (solid line) and $n_{2DEG}=5\times10^{11}$ cm^{-2} (dashed line).

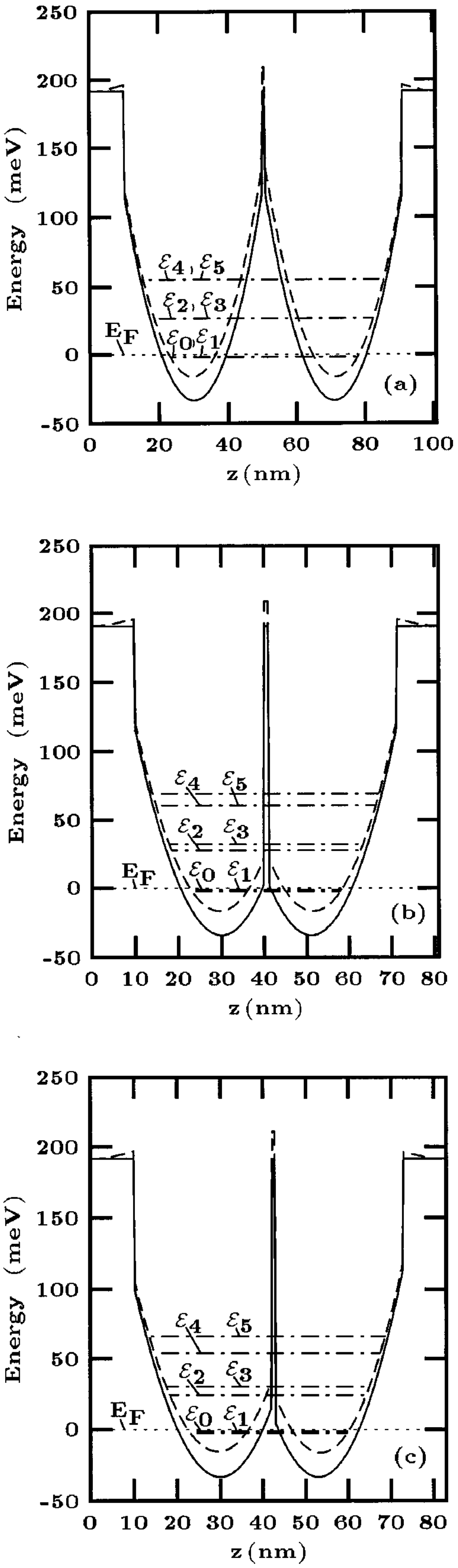

FIG. 5. Bare potential (solid line), effective potential (dashed lined), subband energies (dashed-dotted line), and Fermi energy (dotted line) of a DPQW: (a) symmetric DPQW, (b) symmetric truncated DPQW, (c) asymmetric truncated DPQW. The Fermi energy (dotted line) is chosen to be $E_F=0$.

splitting decreases with increasing electron density, as seen from Fig. 7(b). It is seen from Fig. 8(b), where the density profile for the symmetric truncated DPQW is plotted, that the electrons of both QW's tunnel through the barrier and thus, form one Q2DEG.

The spatial symmetry is broken in the case of the asymmetric truncated DPQW, which is now under consideration. The bare and effective potential and the six lowest subbands are plotted for this DPQW in Fig. 5(c). The asymmetry increases the splitting of the doublets [cf. with Fig. 5(b)], which decreases with increasing electron concentration, as seen from Fig. 7(c). The density profile, plotted in Fig. 8(c), manifests the asymmetry of the confining potential.

III. DENSITY RESPONSE OF THE Q2DEG IN SPQW'S AND DPQW'S

In this section we calculate the response of an electron gas, quantum-confined in a one-dimensional potential acting in the z direction of the sample, to an external applied potential on a quantum-mechanical level, i.e., we consider the density response. Here, we develop the RPA, using the self-consistent field (SCF) method.[30] The obtained result for the dispersion relation of the Q2D plasmons allows the calculation of the dispersion curves in conjunction with the self-consistent calculated ground state of the SPQW's and DPQW's.

The single-particle Hamiltonian of the Q2DEG in the presence of the perturbation is written as $H=H_0+H_1$, where H_0 is the unperturbed single-particle Hamiltonian in the Hartree approximation, which satisfies the effective Schrödinger equation $H_0|K\mathbf{k}_\parallel\rangle=\mathcal{E}_K(\mathbf{k}_\parallel)|K\mathbf{k}_\parallel\rangle$ [cf. Eq. (4)] and $H_1=V^{sc}(\mathbf{x},t)$ is the self-consistent potential. The self-consistent potential is a sum of the external potential $V^{ext}(\mathbf{x},t)$ and the induced potential $V^{ind}(\mathbf{x},t)$. The source of the induced potential is the induced electron density $n_{ind}(\mathbf{x},t)$ resulting from the redistribution of the electrons of the Q2DEG in the presence of $V^{ext}(\mathbf{x},t)$. Assuming that the external potential is switched on adiabatically at $t=-\infty$, we have $V^{ext}(\mathbf{x},t)=V^{ext}(\mathbf{x},\omega)\exp[-i(\omega+i\delta)]$ with $\delta\to 0^+$, the SCF method relates the induced electron density to the self-consistent potential by

$$n_{ind}(\mathbf{x},\omega)=\int d^3x' P^{(1)}(\mathbf{x},\mathbf{x}'|\omega)V^{sc}(\mathbf{x}',\omega), \qquad (16)$$

where $P^{(1)}(\mathbf{x},\mathbf{x}'|\omega)$ is the irreducible (proper) RPA polarization function of the Q2DEG:

$$P^{(1)}(\mathbf{x},\mathbf{x}'|\omega)=\frac{1}{A}\sum_{\mathbf{q}_\parallel} e^{i\mathbf{q}_\parallel\cdot(\mathbf{x}_\parallel-\mathbf{x}'_\parallel)}P^{(1)}(\mathbf{q}_\parallel;z,z'|\omega), \qquad (17)$$

where

$$P^{(1)}(\mathbf{q}_\parallel;z,z'|\omega)=\sum_{KK'} P^{(1)}_{KK'}(\mathbf{q}_\parallel,\omega)\,\eta_{KK'}(z)\,\eta^*_{KK'}(z') \qquad (18)$$

and

$$P^{(1)}_{KK'}(\mathbf{q}_\parallel,\omega)=\frac{2}{A}\sum_{\mathbf{k}_\parallel}\frac{n_F(\mathcal{E}_{K'}(\mathbf{k}_\parallel))-n_F(\mathcal{E}_K(\mathbf{k}_\parallel+\mathbf{q}_\parallel))}{\hbar(\omega+i\delta)+\mathcal{E}_{K'}(\mathbf{k}_\parallel)-\mathcal{E}_K(\mathbf{k}_\parallel+\mathbf{q}_\parallel)} \tag{19}$$

is the RPA matrix polarization function. Here, we have defined

$$\eta_{KK'}(z)=\varphi_K(z)\varphi^*_{K'}(z). \tag{20}$$

In the density-response scheme retardation effects are neglected and thus, the induced potential, which is an induced Hartree potential, is related to the induced density by Poisson's equation. Neglecting image effects, describing the dielectric screening of the background within the ε_s approximation, and exploiting the translation symmetry in the x-y plane by two-dimensional Fourrier series, one obtains

$$\begin{aligned}V^{sc}(\mathbf{q}_\parallel,z|\omega)&=V^{ext}(\mathbf{q}_\parallel,z|\omega)\\&\quad+\frac{e^2}{2\varepsilon_0\varepsilon_s q_\parallel}\int dz'\int dz'' e^{-q_\parallel|z-z'|}\\&\quad\times P^{(1)}(\mathbf{q}_\parallel;z',z''|\omega)V^{sc}(\mathbf{q}_\parallel,z''|\omega).\end{aligned} \tag{21}$$

Performing matrix elements of this equation with the envelope wave functions of Eq. (4) and defining the collective excitations in the usual form as resonances of the Q2DEG to V^{ext}, i.e., collective excitations exist under the condition $V^{ext}=0$ while $V^{sc}\neq 0$, the dispersion relation of the Q2D plasmons results

$$\det[\delta_{K_1K}\delta_{K_2K'}-V^s_{K_1K_2K'K}(\mathbf{q}_\parallel)P^{(1)}_{KK'}(\mathbf{q}_\parallel,\omega)]=0. \tag{22}$$

The Coulomb matrix element is defined by

$$V^s_{K_1K_2K'K}(\mathbf{q}_\parallel)=\frac{e^2}{2\varepsilon_0\varepsilon_s q_\parallel}f^C_{K_1K_2K'K}(\mathbf{q}_\parallel), \tag{23}$$

where the form factor is given by

$$f^C_{K_1K_2K'K}(\mathbf{q}_\parallel)=\int dz\int dz'\,\eta^*_{K_1K_2}(z)e^{-q_\parallel|z-z'|}\eta^*_{K'K}(z'). \tag{24}$$

The real part of the RPA matrix polarization function is[6]

$$\begin{aligned}\mathrm{Re}\,P^{(1)}_{KK'}(\mathbf{q}_\parallel,\omega)&=\frac{m_e k_F^{(K)}}{\pi\hbar^2 q_\parallel}\{-\overline{\eta}_{K'K+}+\mathrm{sgn}(\overline{\eta}_{K'K+})\\&\quad\times\Theta(\overline{\eta}_{K'K+}-1)\sqrt{\overline{\eta}^2_{K'K+}-1}\}\\&\quad+\frac{m_e k_F^{(K')}}{\pi\hbar^2 q_\parallel}\{\overline{\eta}_{KK'-}-\mathrm{sgn}(\overline{\eta}_{KK'-})\\&\quad\times\Theta(\overline{\eta}^2_{KK'-}-1)\sqrt{\overline{\eta}^2_{KK'-}-1}\}\end{aligned} \tag{25}$$

and the imaginary part reads

$$\begin{aligned}\mathrm{Im}P^{(1)}_{KK'}(\mathbf{q}_\parallel,\omega)&=\frac{m_e}{\pi\hbar^2 q_\parallel}\{k_F^{(K)}\Theta(1-\overline{\eta}^2_{K'K+})\sqrt{1-\overline{\eta}^2_{K'K+}}\\&\quad-k_F^{(K')}\Theta(1-\overline{\eta}^2_{KK'-})\sqrt{1-\overline{\eta}^2_{KK'-}},\end{aligned} \tag{26}$$

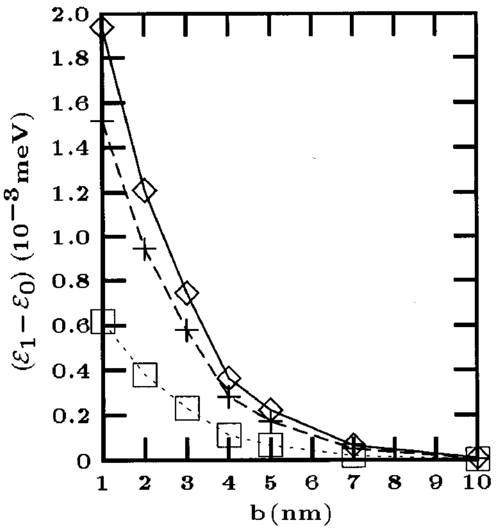

FIG. 6. Subband separation $\mathcal{E}_1-\mathcal{E}_0$ as a function of the barrier thickness b of the DPQW for three different electron number densities: $n_{2DEG}=1\times10^7$ cm^{-2} (solid line), $n_{2DEG}=1\times10^{11}$ cm^{-2} (dashed line), and $n_{2DEG}=5\times10^{11}$ cm^{-2} (dotted line).

with

$$\overline{\eta}_{K'K\pm}=\frac{\omega\pm\Omega_{KK'}}{q_\parallel v_F^{(K')}}\pm\frac{q_\parallel}{2k_F^{(K')}}. \tag{27}$$

The RPA matrix polarization function has the symmetry properties $P^{(1)}_{KK'}(\mathbf{q}_\parallel,\omega)=P^{(1)}_{KK'}(-\mathbf{q}_\parallel,\omega)$, $\mathrm{Re}P^{(1)}_{KK'}(\mathbf{q}_\parallel,\omega)=\mathrm{Re}P^{(1)}_{K'K}(\mathbf{q}_\parallel,-\omega)$, and $\mathrm{Im}P^{(1)}_{KK'}(\mathbf{q}_\parallel,\omega)=\mathrm{Im}P^{(1)}_{K'K}(\mathbf{q}_\parallel,-\omega)$. Further, for the Coulomb matrix elements $V^s_{K_1K_2K_3K_4}(\mathbf{q}_\parallel)=V^s_{K_2K_1K_3K_4}(\mathbf{q}_\parallel)=V^s_{K_1K_2K_4K_3}(\mathbf{q}_\parallel)=V^s_{K_2K_1K_4K_3}(\mathbf{q}_\parallel)=V^s_{K_3K_4K_1K_2}(\mathbf{q}_\parallel)$ is valid, because the wave functions of bound states are always pure real functions. On account of these properties we can restrict the further considerations to the quadrant $\omega>0$ and $q_\parallel>0$ in the ω-$q_\parallel$ plane.

The regions in the ω-$q_\parallel$ plane, where $\mathrm{Im}P^{(1)}_{KK'}(\mathbf{q}_\parallel,\omega)\neq 0$ define the regions, where the single-particle excitations exist, i.e., SPE's have a continuous excitation spectrum, the single-particle continuum. According to the size quantization the SPE's are split in single-particle intrasubband excitations and single-particle intersubband excitations, associated with incoherent electron motion within one and between two different subbands, respectively. Nonvanishing $\mathrm{Im}P^{(1)}_{KK'}(\mathbf{q}_\parallel,\omega)$ indicates that damping is possible even in the absence of collisions, i.e., the Q2D plasmons become Landau damped inside the single-particle continua. The boundaries of these continua are given by

$$\omega^{KK'}_{1,2}=\left|\pm\frac{\hbar k_F^{(K')}}{m_e}+\frac{\hbar q_\parallel^2}{2m_e}+\Omega_{KK'}\right| \tag{28}$$

and

$$\omega^{KK'}_{3,4}=\left|\pm\frac{\hbar k_F^{(K)}}{m_e}-\frac{\hbar q_\parallel^2}{2m_e}+\Omega_{KK'}\right|. \tag{29}$$

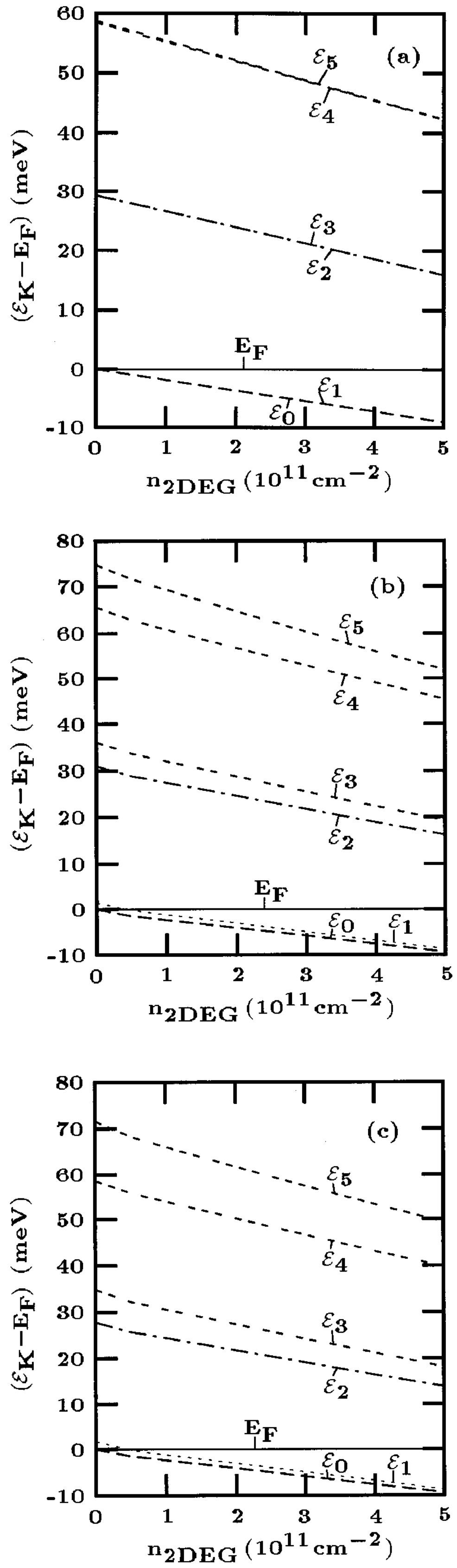

FIG. 7. Subband energies of the symmetric DPQW (a), the symmetric truncated DPQW (b), and the asymmetric truncated DPQW (c) in dependence on the electron number density. The Fermi energy (solid line) is chosen to be $E_F = 0$.

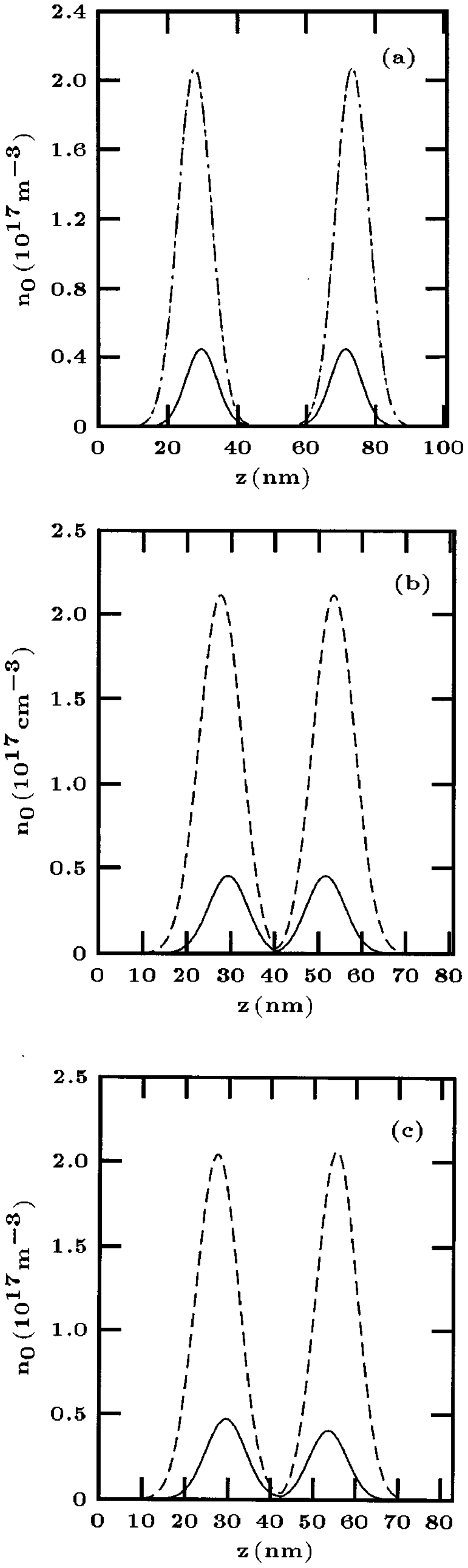

FIG. 8. Electron density profiles of the symmetric DPQW (a), the symmetric truncated DPQW (b), and the asymmetric truncated DPQW (c) for $n_{2DEG} = 1 \times 10^{11}$ cm^{-2} (solid line) and $n_{2DEG} = 5 \times 10^{11}$ cm^{-2} (dashed line).

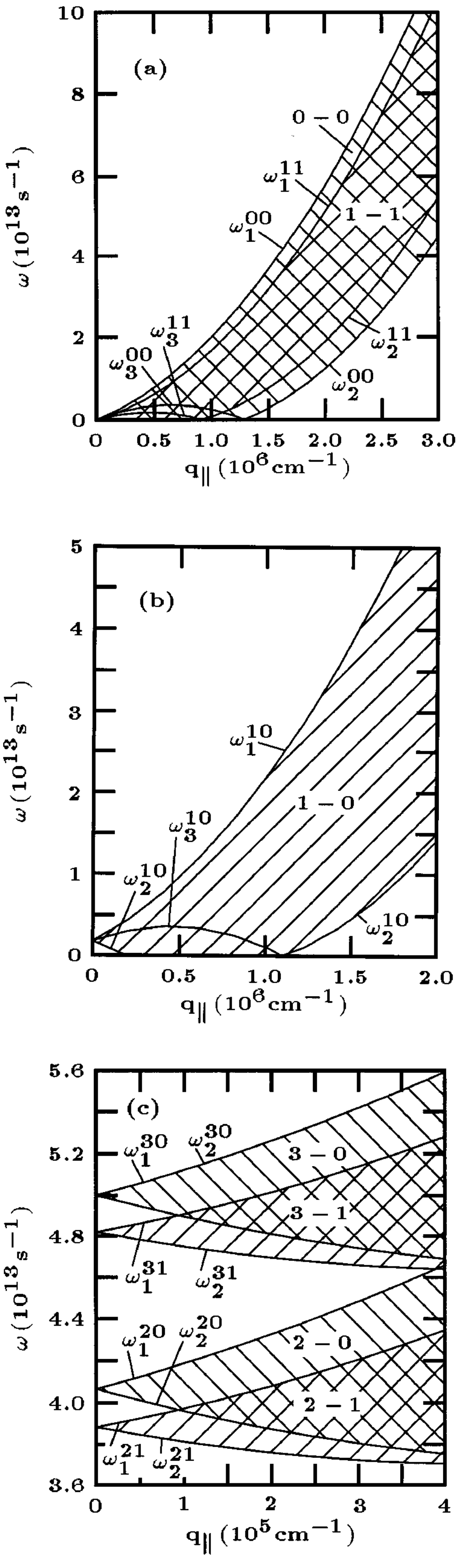

FIG. 9. Single-particle continua of a Q2DEG for a four-subband model assuming that two subbands are occupied: single-particle $(0-0)$ and $(1-1)$ intrasubband continua (a), single-particle $(1-0)$ intersubband continuum (b), and single-particle $(2-1)$, $(2-0)$, $(3-1)$, and $(3-0)$ intersubband continua (c).

The single-particle continua of a Q2DEG assuming four subbands ($K=0,1,2,3$) from which two are occupied are plotted in Fig. 9. According to the different single-electron motions within the occupied subbands, $0\leftrightarrow 0$, $1\leftrightarrow 1$ [Fig. 9(a)], and between the different subbands considered here, $0\leftrightarrow 1$ [Fig. 9(b)], $1\leftrightarrow 2$, $0\leftrightarrow 2$, $1\leftrightarrow 3$, and $0\leftrightarrow 3$ [Fig. 9(c)] seven single-particle intra- and intersubband continua arise. Each single-particle $(K-K')$ intersubband continuum starts at $q_\parallel=0$ at the corresponding subband separation frequency $\Omega_{KK'}$. Because the RPA scheme considers the response of noninteracting electrons on the self-consistent potential, the different SPE's are independent.

In difference to the SPE's, the Q2D plasmons are accompanied in general by different collective intra- and intersubband transitions (coherent electron motion), i.e., intersubband coupling (ISC) is present and thus, the resulting spectrum is of hybrid type concerning the associated intra- and intersubband transitions. If the confining potential is spatial symmetric it follows $V^s_{K_1K_2K_3K_4}=0$ if $K_1+K_2+K_3+K_4=$odd number and thus, the dispersion relation separates in one describing symmetric Q2D plasmons

$$\det[\delta_{mn}\delta_{K_2K}-V^s_{K_2+2mK_2K+2nK}(\mathbf{q}_\parallel)\chi^{(1)}_{K+2nK}(\mathbf{q}_\parallel,\omega)]=0 \tag{30}$$

and the other describes antisymmetric Q2D plasmons

$$\det[\delta_{mn}\delta_{K_2K}-V^s_{K_2+(2m+1)K_2K+(2n+1)K}(\mathbf{q}_\parallel)\times\chi^{(1)}_{K+(2n+1)K}(\mathbf{q}_\parallel,\omega)]=0, \tag{31}$$

where we have used the symmetry properties of $V^s_{K_1K_2K_3K_4}$ and have defined

$$\chi^{(1)}_{KK'}(\mathbf{q}_\parallel,\omega)=\frac{P^{(1)}_{KK'}(\mathbf{q}_\parallel,\omega)+P^{(1)}_{K'K}(\mathbf{q}_\parallel,\omega)}{1+\delta_{KK'}} \tag{32}$$

and it is $n,m=0,1,2,\ldots$. Equation (30) describes Q2D plasmons which are connected with the collective electron transitions between states with the same parity (even parity modes), whereas Eq. (31) describes Q2D plasmons connected with collective electron transitions between states with opposite parity (odd parity modes).

In the case of weak ISC one can apply the diagonal approximation: $V^s_{K_1K_2K_3K_4}=\delta_{K_1K_3}\delta_{K_2K_4}V^s_{K_1K_2K_1K_2}$. In this case the dispersion relation, Eq. (22), reads

$$1-V^s_{K'KK'K}(\mathbf{q}_\parallel)\chi^{(1)}_{KK'}(\mathbf{q}_\parallel,\omega)=0, \tag{33}$$

which describes (i) for $K=K'$ the $(K-K)$ intrasubband plasmon ω_p^{KK}, if the collective electron transition is within the subband $\mathcal{E}_K$ and (ii) for $K\neq K'$ the $(K-K')$ intersubband plasmon $\omega_p^{KK'}$ if the collective intersubband transition is between the subbands $\mathcal{E}_{K'}\leftrightarrow\mathcal{E}_K$.

The classification of the modes in intra- and intersubband plasmons is strictly valid only for vanishing ISC. Starting from this picture the ISC results in a hybrid-type spectrum. In many cases the ISC is weak and then each resulting branch of hybrid (coupled or mixed) mode is dominated by one collective electron motion only. In this case it is profitable to denote the modes by $\omega_p^{KK'}$.

Fortunately, the number of algebraic equations determining the dispersion curves of the Q2D plasmons is restricted to a small number $K,K'=0,1,2,\ldots,N-1$, because $P^{(1)}_{KK'}(\mathbf{q}_\parallel,\omega)\rightarrow 0$ if $|K-K'|$ becomes a large number. Further, $P^{(1)}_{KK'}(\mathbf{q}_\parallel,\omega)=0$ if both inequalities, $E_F\leqslant\mathcal{E}_K$ and $E_F\leqslant\mathcal{E}_{K'}$ are valid and in typical Q2D structures only one or two subbands are occupied. Thus, it is possible to restrict to a finite number N of subbands, i.e., one can use a multisubband model (N-subband model). For practical calculations we use in the case of the SPQW a two-subband model: $K,K'=0,1$ and for the DPQW's a four-subband model: $K,K'=0,1,2,3$. For a two-subband model Eq. (22) takes the form

$$\begin{vmatrix} 1-V^s_{0000}\chi^{(1)}_{00} & V^s_{0010}\chi^{(1)}_{10} & V^s_{0011}\chi^{(1)}_{11} \\ V^s_{1000}\chi^{(1)}_{00} & 1-V^s_{1010}\chi^{(1)}_{10} & V^s_{1011}\chi^{(1)}_{11} \\ V^s_{1100}\chi^{(1)}_{00} & V^s_{1110}\chi^{(1)}_{10} & 1-V^s_{1111}\chi^{(1)}_{11} \end{vmatrix}=0, \tag{34}$$

which splits for a mirror-symmetric effective confining potential in

$$[1-V^s_{0000}(\mathbf{q}_\parallel)\chi^{(1)}_{00}(\mathbf{q}_\parallel,\omega)][1-V^s_{1111}(\mathbf{q}_\parallel)\chi^{(1)}_{11}(\mathbf{q}_\parallel,\omega)] - V^s_{0011}(\mathbf{q}_\parallel)V^s_{1100}(\mathbf{q}_\parallel)\chi^{(1)}_{00}(\mathbf{q}_\parallel,\omega)\chi^{(1)}_{11}(\mathbf{q}_\parallel,\omega)=0, \tag{35}$$

describing the symmetric Q2D plasmons and in

$$1-V^s_{1010}(\mathbf{q}_\parallel)\chi^{(1)}_{10}(\mathbf{q}_\parallel,\omega)=0 \tag{36}$$

describing the antisymmetric modes. Please note that $\chi^{(1)}_{11}=0$ if only the lowest subband is occupied, i.e., in the electric quantum limit (EQL). In this case Eq. (35) describes $(0-0)$ intrasubband plasmons, accompanied by collective electron motion in subband $\mathcal{E}_0(\mathbf{k}_\parallel)$ and Eq. (36) describes $(1-0)$ intersubband plasmons, accompanied by collective electron motions between subbands $\mathcal{E}_0(\mathbf{k}_\parallel)$ and $\mathcal{E}_1(\mathbf{k}_\parallel)$.

In the case of a four-subband model, assuming two subbands to be occupied, the Q2D plasmon dispersion relation reads

$$\begin{vmatrix} 1-V^s_{0000}\chi^{(1)}_{00} & V^s_{0010}\chi^{(1)}_{10} & V^s_{0020}\chi^{(1)}_{20} & V^s_{0030}\chi^{(1)}_{30} & V^s_{0011}\chi^{(1)}_{11} & V^s_{0021}\chi^{(1)}_{21} & V^s_{0031}\chi^{(1)}_{31} \\ V^s_{1000}\chi^{(1)} & 1-V^s_{1010}\chi^{(1)}_{10} & V^s_{1020}\chi^{(1)}_{20} & V^s_{1030}\chi^{(1)}_{30} & V^s_{1011}\chi^{(1)}_{11} & V^s_{1021}\chi^{(1)}_{21} & V^s_{1031}\chi^{(1)}_{31} \\ V^s_{2000}\chi^{(1)}_{00} & V^s_{2010}\chi^{(1)}_{10} & 1-V^s_{2020}\chi^{(1)}_{20} & V^s_{2030}\chi^{(1)}_{30} & V^s_{2011}\chi^{(1)}_{11} & V^s_{2021}\chi^{(1)}_{21} & V^s_{2031}\chi^{(1)}_{31} \\ V^s_{3000}\chi^{(1)}_{00} & V^s_{3010}\chi^{(1)}_{10} & V^s_{3020}\chi^{(1)}_{20} & 1-V^s_{3030}\chi^{11}_{30} & V^s_{3011}\chi^{(1)}_{11} & V^s_{3021}\chi^{(1)}_{21} & V^s_{3031}\chi^{(1)}_{31} \\ V^s_{1100}\chi^{(1)}_{00} & V^s_{1110}\chi^{(1)}_{10} & V^s_{1120}\chi^{(1)}_{20} & V^s_{1130}\chi^{(1)}_{30} & 1-V^s_{1111}\chi^{(1)}_{11} & V^s_{1121}\chi^{(1)}_{21} & V^s_{1131}\chi^{(1)}_{31} \\ 1-V^s_{2100}\chi^{(1)}_{00} & V^s_{2110}\chi^{(1)}_{10} & V^s_{2120}\chi^{(1)}_{20} & V^s_{2130}\chi^{(1)}_{30} & V^s_{2111}\chi^{(1)}_{11} & 1-V^s_{2121}\chi^{(1)}_{21} & V^s_{2131}\chi^{(1)}_{31} \\ V^s_{3100}\chi^{(1)}_{00} & V^s_{3110}\chi^{(1)}_{10} & V^s_{3120}\chi^{(1)}_{20} & V^s_{3130}\chi^{(1)}_{30} & V^s_{3111}x^{(1)}_{11} & V^s_{3121}\chi^{(1)}_{21} & 1-V^s_{3131}\chi^{(1)}_{31} \end{vmatrix}=0, \tag{37}$$

which separates in the determinantal dispersion relation

$$\begin{vmatrix} 1-V^s_{0000}\chi^{(1)}_{00} & V^s_{0020}\chi^{(1)}_{20} & V^s_{0011}\chi^{(1)}_{11} & V^s_{0031}\chi^{(1)}_{31} \\ V^s_{2000}\chi^{(1)}_{00} & 1-V^s_{2020}\chi^{(1)}_{20} & V^s_{2011}\chi^{(1)}_{11} & V^s_{2031}\chi^{(1)}_{31} \\ V^s_{1100}\chi^{(1)}_{00} & V^s_{1120}\chi^{(1)}_{20} & 1-V^s_{1111}\chi^{(1)}_{11} & V^s_{1131}\chi^{(1)}_{31} \\ V^s_{3100}\chi^{(1)}_{00} & V^s_{3120}\chi^{(1)}_{20} & V^s_{3111}\chi^{(1)}_{11} & 1-V^s_{3131}\chi^{(1)}_{31} \end{vmatrix}=0 \tag{38}$$

describing the symmetric Q2D plasmons and those determining the antisymmetric Q2D plasmons

$$\begin{vmatrix} 1-V^s_{1010}\chi^{(1)}_{10} & V^s_{1030}\chi^{(1)}_{30} & V^s_{1021}\chi^{(1)}_{21} \\ V^s_{3010}\chi^{(1)}_{10} & 1-V^s_{3030}\chi^{(1)}_{30} & V^s_{3021}\chi^{(1)}_{21} \\ V^s_{2110}\chi^{(1)}_{10} & V^s_{2130}\chi^{(1)}_{30} & 1-V^s_{2121}\chi^{(1)}_{21} \end{vmatrix}=0, \tag{39}$$

if the effective confining potential is mirror symmetric. Equations (37)–(39) describe hybrid-type modes, i.e., Eq. (37) determines seven branches of dispersion curves of $(0-0)$ and $(1-1)$ intrasubband plasmons and $(1-0)$, $(2-1)$, $(2-0)$, $(3-1)$, and $(3-0)$ intersubband plasmons, denoted by ω^{00}_p, ω^{11}_p, ω^{10}_p ,ω^{21}_p, ω^{20}_p, ω^{31}_p, and ω^{30}_p, respectively. Equation (38) describes the four symmetric branches ω^{00}_p, ω^{11}_p, ω^{20}_p, and ω^{31}_p, and Eq. (39) determines the three antisymmetric branches ω^{10}_p, ω^{21}_p, and ω^{30}_p. That means we denote each branch by the mainly contributing collective intra- or intersubband transition as long as the ISC is weak.

IV. SELF-CONSISTENT CALCULATION OF Q2D PLASMONS IN SPQW'S AND DPQW'S

In this chapter we represent numerical results of the RPA dispersion relations of the Q2D plasmons using the self-

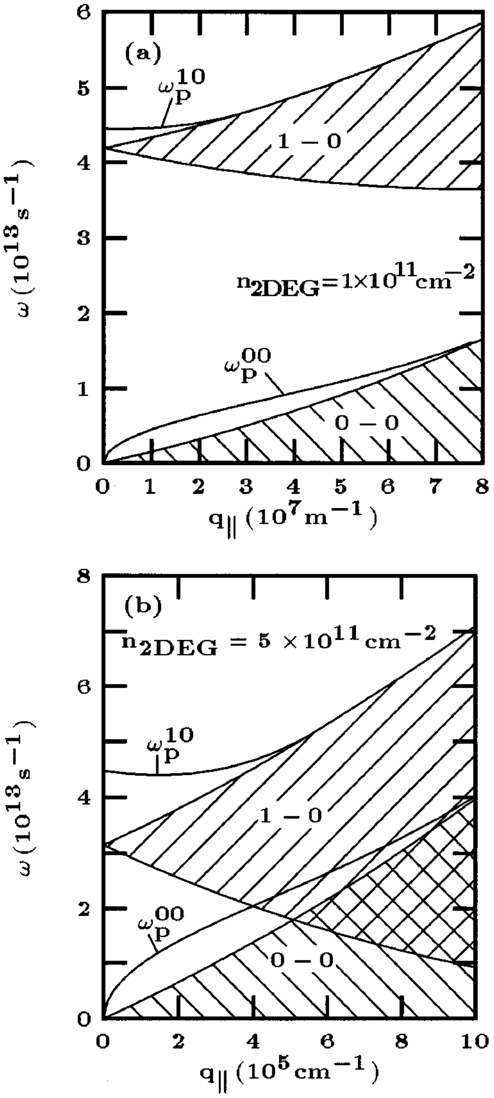

FIG. 10. Dispersion relation of the Q2D plasmons of the SPQW calculated self-consistently in RPA in dependence on the wave vector component $q_\parallel$: (a) $n_{2DEG}=1\times10^{11}$ cm^{-2}, (b) $n_{2DEG}=5\times10^{11}$ cm^{-2}. The hatched areas correspond to the single-particle continua with boundaries $\omega_{1,2}^{KK'}$ and $\omega_{3,4}^{KK'}$.

consistent calculated ground state of the SPQW's and DPQW's.

A. Q2D plasmons of SPQW's

In the case of the SPQW's considered in Sec. II B the RPA dispersion relations are given in general by Eqs. (30) and (31). Because only the lowest subband is occupied it is sufficient to use a two-subband model and thus, we have to use Eq. (35) with $\chi_{11}^{(1)}=0$ for the symmetric Q2D plasmon ω_p^{00} and Eq. (36) to determine the dispersion curve of the antisymmetric Q2D plasmon ω_p^{10}.

The full RPA dispersion curves of the Q2D plasmons of a SPQW are plotted in Fig. 10 in dependence on the wave vector component $q_\parallel$. Note, that for both chosen electron densities only one subband is occupied. Within this model each plotted branch is accompanied by only one type of collective electron transition: ω_p^{00} is associated by collective electron motion in the lowest subband and thus, is a pure $(0-0)$ intrasubband plasmon and ω_p^{10} is associated by collective electron transition between the two subbands under consideration and thus, is a pure $(1-0)$ intersubband plasmon. The dispersion curve of the intrasubband plasmon starts at $q_\parallel=0$ and $\omega=0$ and enters for larger wave vectors the single-particle $(0-0)$ intrasubband continuum. Because of the symmetry the intrasubband plasmon ω_p^{00} is not Landau damped within the single-particle $(1-0)$ intersubband continuum [see Fig. 10(b)]. Further, it is seen from Fig. 10 that the $(1-0)$ intersubband plasmon starts for $q_\parallel=0$ above the subband separation frequency $\Omega_{10}<\omega_p^{10}$. This frequency shift, $\Delta_p^{10}=\omega_p^{10}(q_\parallel=0)-\Omega_{10}$ is the depolarization shift. This many-particle effect arises because each electron ''feels'' a field which is different from the unscreened field (resonance screening), i.e., if the electron gas oscillates in the mode ω_p^{10} the arising induced electron density changes the Hartree potential. The both collective modes, ω_p^{00} and ω_p^{10}, under consideration are plotted in dependence on the electron number density of the Q2DEG in Fig. 11. The fully self-consistent calculations of the ground state and the response show that ω_p^{00} $(q_\parallel\neq0)$ has an increasing frequency with increasing density. This increase is larger than that of the upper boundary ω_1^{00} of the $(0-0)$ SPE continuum. The corresponding dispersion curves of the $(1-0)$ intersubband plasmon ω_p^{10} are depicted in Figs. 11(b) and 11(c). It is seen from Fig. 11(b) that for $q_\parallel=0$ the mode ω_p^{10} is nearly pinned at a frequency slightly above the subband separation frequency $\Omega_{10}(n_{2DEG}=0)\equiv\Omega$ of the bare confining potential in the plotted range of n_{2DEG}. This is nothing else but the manifestation of the generalized Kohn's theorem[22] in the spectrum of the Q2D plasmons. For a bare perfect parabolic potential the generalized Kohn's theorem gives exactly that far-infrared light is absorbed by the quantum-confined electron gas at the confining frequency Ω of the bare parabolic potential, independent from the electron-electron interaction and the number of electrons in the PQW. Thus, the only dipole-active mode is ω_p^{10} and is called Kohn's mode. The small deviation appearing in Fig. 11(b) results from the deviation of the chosen truncated SPQW from a perfect SPQW. This theorem, considered from the viewpoint of many-particle physics, states the exact cancellation of the Hartree renormalization (tadpole self-energy diagrams) of the subband separation frequency $\Delta\Omega_{10}=\Omega_{10}(0)-\Omega_{10}(n_{2DEG})$ with the depolarization shift $\Delta_p^{10}=\omega_p^{10}(q_\parallel=0)-\Omega_{10}(n_{2DEG})$: $\omega_p^{10}(q_\parallel=0)=\Omega_{10}(0)$ only if $\Delta_p^{10}=\Delta\Omega_{10}$. Whereas Kohn's theorem states that the absorption spectrum has only one peak at $\omega=\Omega$, the mode spectrum of the freely oscillating Q2DEG consists of all types of Q2D modes. The mode spectrum of a Q2DEG is universal, i.e., the types of the appearing modes are independent from the concrete shape of the confining potential. The confining potential only influences details of this mode spectrum. Please note that for $q_\parallel=0$ the single-particle $(1-0)$ continuum degenerates to the line $\omega_1^{10}=\omega_2^{10}=\Omega_{10}$. It is seen that ω_1^{10} decreases with increasing electron density n_{2DEG} and thus, with increasing n_{2DEG} the depolarization shift Δ_p^{10} increases. From Fig.

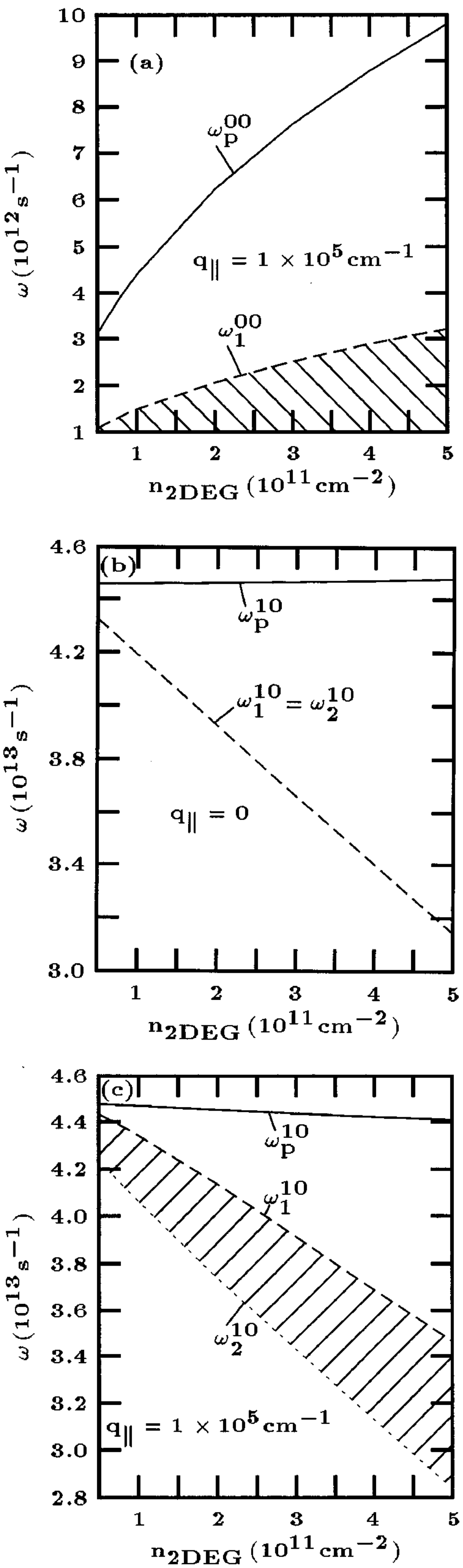

FIG. 11. Dispersion relation of the $(0-0)$ intrasubband plasmon ω_p^{00} (solid line) for $q_{\|}=1\times10^5$ cm^{-1} (a) and of the $(1-0)$ intersubband plasmon ω_p^{10} (solid line) for $q_{\|}=0$ (b) and for $q_{\|}=1\times10^5$ cm^{-1} (c) of the SPQW calculated self-consistently in RPA in dependence on the electron number density. The hatched areas correspond to the single-particle continua with boundaries ω_1^{00} (dashed line) (a), ω_1^{10} (dashed line) and ω_2^{10} (dotted line) (b) and (c).

11(c), where ω_p^{10} is plotted in dependence on the electron density, it becomes obvious that for $q_{\|}\neq0$ the frequency of ω_p^{10} depends on the electron density, i.e., it decreases with increasing electron concentration. It is seen that the boundaries of the SPE continuum ω_1^{10} and ω_2^{10} decrease more rapidly with increasing electron density as ω_p^{10}.

B. Q2D plasmons of DPQW's

1. Symmetric DPQW

Let us now discuss the Q2D plasmons of the symmetric DPQW. In this case we use a four-subband model. The full RPA dispersion curves of the symmetric DPQW [cf. Figs. 5(a), 7(a), and 8(a) for the ground state] calculated from Eq. (38): ω_p^{00}, ω_p^{11}, ω_p^{20}, ω_p^{31}, and from Eq. (39): ω_p^{10}, ω_p^{21}, and ω_p^{30} are plotted in Figs. 12(a)–12(c). In the case considered here two subbands are occupied and thus, two branches of intrasubband plasmons appear: ω_p^{00} and ω_p^{11}. These two branches are accompanied by the collective electron transitions $0\leftrightarrow0$, $1\leftrightarrow1$ and $0\leftrightarrow2$, $1\leftrightarrow3$, which are coupled due to ISC effects. Because the frequencies of the $(2-0)$ and $(3-1)$ intersubband plasmons are large in comparison to the frequencies of the intrasubband plasmons, we can separate these collective motions from the intrasubband motion in subbands $\mathcal{E}_0$ and $\mathcal{E}_1$. Thus, in a very good approximation the branches ω_p^{00} and ω_p^{11} are determined by the following dispersion relation:

$$\begin{vmatrix} 1-V^s_{0000}\chi^{(1)}_{00} & V^s_{0011}\chi^{(1)}_{11} \\ V^s_{1100}\chi^{(1)}_{00} & 1-V^s_{1111}\chi^{(1)}_{11} \end{vmatrix} = 0. \tag{40}$$

If we expand $\chi^{(1)}_{00}(\mathbf{q}_{\|},\omega)$ and $\chi^{(1)}_{11}(\mathbf{q}_{\|},\omega)$ in the lowest order of $q_{\|}$, we obtain

$$\chi^{(1)}_{00}(\mathbf{q}_{\|},\omega) = \frac{N_0 q_{\|}^2}{m_e\omega^2} \tag{41}$$

and

$$\chi^{(1)}_{11}(\mathbf{q}_{\|},\omega) = \frac{N_1 q_{\|}^2}{m_e\omega^2}. \tag{42}$$

Using both expressions in Eq. (40) we find

$$\omega_p^{\pm} = \left\{ \frac{e^2 q_{\|}}{2m_e\varepsilon_0\varepsilon_s} \left[\frac{N_0 f^C_{0000}(\mathbf{q}_{\|}) + N_1 f^C_{1111}(\mathbf{q}_{\|})}{2} \pm \left(\frac{[N_0 f^C_{0000}(\mathbf{q}_{\|}) + N_1 f^C_{1111}(\mathbf{q}_{\|})]^2}{4} - N_0 N_1 \{ f^C_{0000}(\mathbf{q}_{\|}) f^C_{1111}(\mathbf{q}_{\|}) - [f^C_{1100}(\mathbf{q}_{\|})]^2 \} \right)^{1/2} \right] \right\}^{1/2}. \tag{43}$$

Because for $q_{\|}\rightarrow0$ $f^C_{0000}(\mathbf{q}_{\|})\approx f^C_{1100}(\mathbf{q}_{\|})\approx f^C_{1111}(\mathbf{q}_{\|})\rightarrow1$ is valid, we find from Eq. (43)

$$\omega_p^{+} = \left(\frac{n_{2DEG} e^2 q_{\|}}{2m_e\varepsilon_0\varepsilon_s} \right)^{1/2}, \tag{44}$$

$$\omega_p^{-} = 0. \tag{45}$$

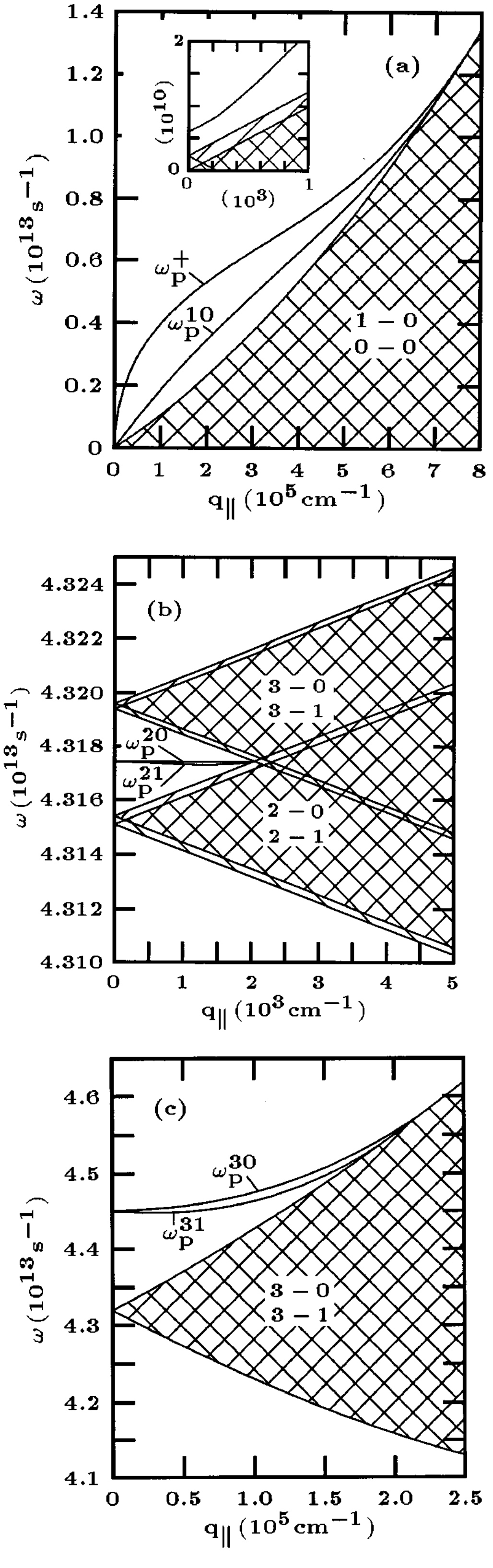

FIG. 12. Dispersion relation of the Q2D plasmons of the symmetric DPQW calculated self-consistently in RPA in dependence on the wave vector component $q_\parallel$ for $n_{2DEG}=1\times10^{11}$ cm^{-2}: (a) ω_p^+ and ω_p^{10}, (b) ω_p^{21} and ω_p^{20}, (c) ω_p^{31} and ω_p^{30}. The hatched areas correspond to the single-particle continua.

From Eq. (44) it becomes obvious that in the long-wavelength approximation (LWA) the mode ω_p^+ behaves like an (uncoupled) $(0-0)$ intrasubband plasmon with density $n_{2DEG}=N_0+N_1$, whereas $\omega_p^-\to 0$ is valid. In the case of the diagonal approximation, i.e., neglecting the ISC in Eq. (40) by setting the nondiagonal elements equal to zero and using Eqs. (41) and (42) the results $\omega_p^+\equiv\omega_p^{00}=[N_0e^2q_\parallel/(2m_e\varepsilon_0\varepsilon_s)]^{1/2}$ and $\omega_p^-\equiv\omega_p^{11}=[N_1e^2q_\parallel/(2m_e\varepsilon_0\varepsilon_s)]^{1/2}$ would appear. But the strong ISC makes the diagonal approximation inadequate, and thus we denote the intrasubband branches by $\omega_p^\pm$ instead of ω_p^{00} and ω_p^{11}. Whereas the mode ω_p^+ is outside of the SPE continua, ω_p^- appears within the single-particle intrasubband continuum. Thus, ω_p^- is highly damped by the resonant and collisionless mechanism of the Landau damping and not plotted in Fig. 12(a). The antisymmetric mode ω_p^{10} is associated with all antisymmetric intersubband transitions, but dominated by the collective transition $0\leftrightarrow 1$. Thus, this branch is an intersubband mode with a nonvanishing depolarization shift [see inset of Fig. 12(a)]. The single-particle $(0-0)$, $(1-0)$, and $(1-1)$ continua overlap nearly entirely. It is important to note that ω_p^+ crosses ω_p^{10} because of the different symmetries of these modes. The frequency of the intersubband mode ω_p^{10} is very small because of the small subband separation frequency Ω_{10}. For Ω_{10} one obtains $\Omega_{10}=2.29863\times10^9$ s^{-1} at $n_{2DEG}=1\times10^{11}$ cm^{-2} and $\Omega_{10}=9.41767\times10^{10}$ s^{-1} at $n_{2DEG}=5\times10^{11}$ cm^{-2} which is very small compared to the other subband separation frequencies. This is seen from Fig. 12(b), where the SPE continua start at $q_\parallel=0$ from the associated subband separation frequencies. Further, from this figure it is seen that the $(2-1)$ and $(2-0)$ SPE continua on the one side and the $(3-1)$ and $(3-0)$ SPE continua on the other side nearly overlap. It is seen from Fig. 12(b) that the frequencies of the symmetric mode ω_p^{20} and of the antisymmetric mode ω_p^{21} are nearly the same. This is also true because $\Omega_{20}\approx\Omega_{21}$ is valid. As long as the DPQW is mirror symmetric the modes ω_p^{20} and ω_p^{21} are independent and thus may cross. The fully self-consistent calculated RPA dispersion curves of ω_p^{30} and ω_p^{31} are plotted in Fig. 12(c). The mode ω_p^{30} is antisymmetric and ω_p^{31} is symmetric and thus both modes are not coupled. But the ISC between the collective transitions $0\leftrightarrow 3$ and $1\leftrightarrow 2$ on the one side and $1\leftrightarrow 3$ and $0\leftrightarrow 2$ on the other side results in a repelling of these modes. As a result the modes ω_p^{21} and ω_p^{20} appear below the single-particle $(3-0)$ intersubband continuum. Because the region free of Landau damping [see Fig. 12(b)] is restricted on small wave vectors, the modes ω_p^{21} and ω_p^{20} can only exist in this small range of $q_\parallel$.

In Fig. 13 we compare the dispersion curves ω_p^{00} of the SPQW, calculated for $n_{2DEG}=0.5\times10^{11}$ cm^{-2} and $n_{2DEG}=1\times10^{11}$ cm^{-2}, with ω_p^+ of the symmetric DPQW, calculated for $n_{2DEG}=1\times10^{11}$ cm^{-2}. It is seen that for small wave vectors ω_p^+ of the DPQW approaches the dispersion curve of ω_p^{00} of the SPQW with the higher density and for larger wave vectors the dispersion curve calculated with the smaller electron density is asymptotically approached. This result may be interpreted from the fact that the strength of the ISC depends on the wave vector. For small wave vectors the ISC is very strong, so that $\omega_p^+\propto(N_0+N_1)^{1/2}$, i.e., $\omega_p^+=\omega_p^{00}(n_{2DEG})$ is identical to the $(0-0)$ intrasubband plasmon of a SPQW with the same n_{2DEG} as that of the

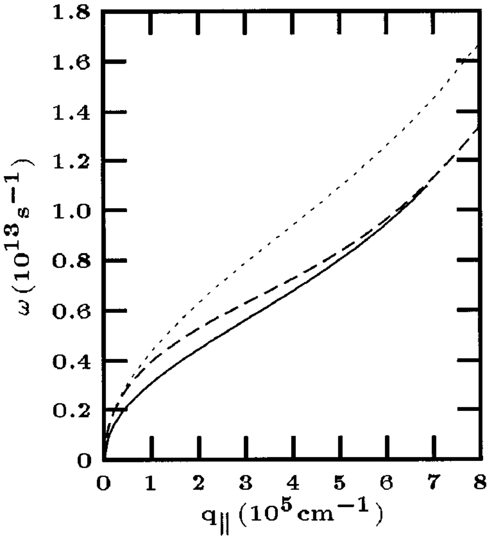

FIG. 13. Dispersion relation of the intrasubband plasmons of the SPQW and of the symmetric DPQW calculated self-consistently in RPA in dependence on the wave vector component $q_{\|}$: ω_p^{00} of the SPQW for $n_{2DEG}=0.5\times10^{11}$ cm^{-2} (solid line) and for $n_{2DEG}=1\times10^{11}$ cm^{-2} (dotted line), and ω_p^+ of the DPQW for $n_{2DEG}=1\times10^{11}$ cm^{-2} (dashed line).

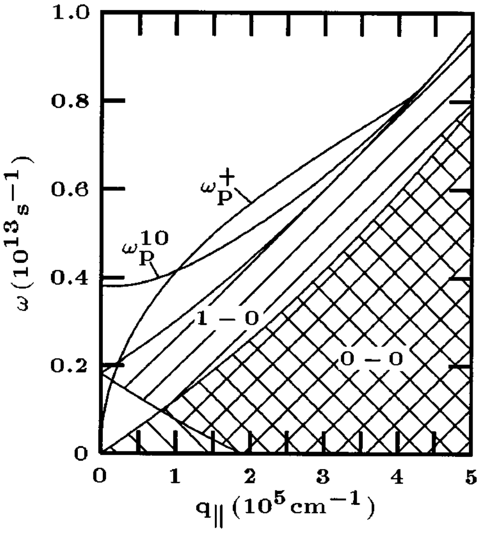

FIG. 14. Dispersion relation of the Q2D plasmons ω_p^+ and ω_p^{10} of the symmetric truncated DPQW calculated self-consistently in RPA in dependence on the wave vector component $q_{\|}$ for $n_{2DEG}=1\times10^{11}$ cm^{-2}. The hatched areas correspond to the single-particle continua.

DPQW. Please note that for the symmetric DPQW the tunneling probability between the two QW's is very weak. Thus, we have two separated PQW's to a good approximation, each filled by $n_{2DEG}/2$ electrons per unit area. With increasing wave vector the ISC decreases and thus, $\omega_p^+ \rightarrow \omega_p^+(N_0)$ which gives $\omega_p^+ = \omega_p^{00}(n_{2DEG}/2)$, i.e., becomes identical to the $(0-0)$ intrasubband plasmon of a SPQW with $n_{2DEG}/2$. This result gives rise to the interpretation from the different point of view of two separated Q2DEG's only coupled via the Coulomb coupling. For $q_{\|}\rightarrow 0$ the two electron systems oscillate strongly coupled and thus, with the density $n_{2DEG}/2+n_{2DEG}/2$ but for larger $q_{\|}$ the Coulomb coupling decreases and thus, the relevant density is $n_{2DEG}/2$. It should be remarked that the here obtained results for two coupled PQW's of finite width generalize the results of Ref. 24 in which the plasmons of two Coulomb coupled strict 2DEG's without tunneling are investigated. In this paper the mode ω_p^- was found to be outside the intrasubband continua if the two 2DEG's are separated larger than a critical value. This is not the case for the here considered parameters of the DPQW.

2. Symmetric truncated DPQW

Now we investigate the symmetric truncated DPQW. Because also in this case two subbands are occupied we use again the four-subband model. As shown in the self-consistent calculations of the ground-state properties, here the splitting of the doublets due to the tunneling from one PQW to the other is larger, so that the subband separation frequencies $\Omega_{KK'}$ are well separated.

The fully self-consistent calculated RPA dispersion curves of the Q2D plasmons of the symmetric truncated DPQW [cf. Figs. 5(b), 7(b), and 8(b) for the ground state] are plotted in Figs. 14 and 15 and are calculated from Eq. (38): ω_p^{00}, ω_p^{11}, ω_p^{20}, ω_p^{31}, and from Eq. (39): ω_p^{10}, ω_p^{21}, and ω_p^{30}. Again the strong ISC causes that the collective intrasubband motion $0\leftrightarrow0$ and $1\leftrightarrow1$ is strongly coupled so that instead of the denotation ω_p^{00} and ω_p^{11} we use $\omega_p^{\pm}$. The numerical calculations show that only ω_p^+ appears outside the intrasubband $(0-0)$ and $(1-1)$ SPE continua. It becomes obvious that in comparison to Fig. 12(a) the frequency of ω_p^{10} crosses ω_p^+ at a larger value of $q_{\|}$. This crossing occurs as long as the DPQW is mirror symmetric. From Figs. 15(a) and 15(b), where the higher-frequency intersubband plasmons are plotted for two different electron densities, it is seen that these modes are well separated. For the lower density the mode ω_p^{21} appears in the small region between the $(2-0)$ and $(2-1)$ SPE continuum, whereas it is above of these two continua for the larger electron density. A similar behavior is observed for ω_p^{31} [cf. Fig. 15(a) with 15(b)]. It is seen that with increasing electron density the separation between the modes decreases. This is caused by the fact that with increasing electron density the coupling between the electrons in both wells of the DPQW decreases and thus the subband separation frequencies $\Omega_{KK'}$ of these doublets decrease.

3. Asymmetric truncated DPQW

In the following we will discuss in detail the asymmetric truncated DPQW. For the calculation of the Q2D plasmon dispersion relation we use a four-subband model from which the two lowest subbands are occupied. Because in this case the effective potential is spatially not mirror symmetric the dispersion curves are calculated from Eq. (37). Thus, all collective intra- and intersubband transitions become coupled. In this case it makes sense only to denote the resulting branches of dispersion curves by ω_p^{00}, ω_p^{11}, ω_p^{10}, ω_p^{21}, ω_p^{20}, ω_p^{31}, and ω_p^{30} if the ISC is not too strong. The fully self-consistent calculated RPA dispersion curves of the Q2D plasmons of the asymmetric truncated DPQW [cf. Figs. 5(c),

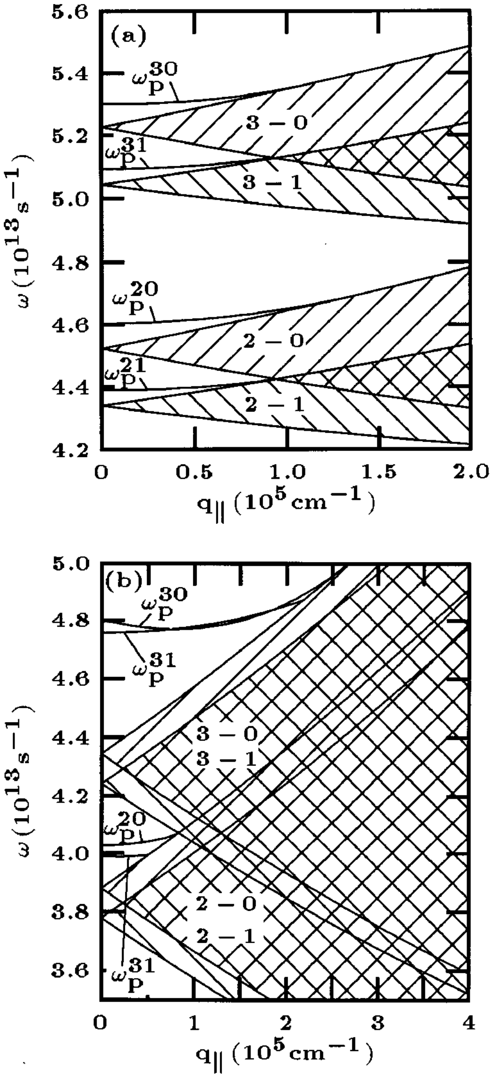

FIG. 15. Dispersion relation of the Q2D plasmons ω_p^{21}, ω_p^{20}, ω_p^{31} and ω_p^{30} of the symmetric truncated DPQW calculated self-consistently in RPA in dependence on the wave vector component $q_\parallel$ for $n_{2DEG}=1\times 10^{11}$ cm^{-2} (a) and for $n_{2DEG}=5\times 10^{11}$ cm^{-2} (b). The hatched areas correspond to the single-particle continua.

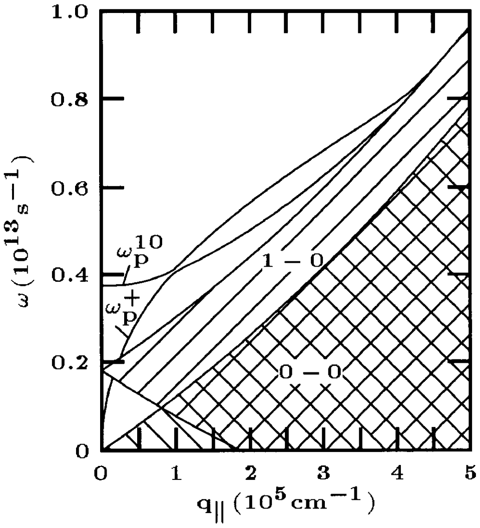

FIG. 16. Dispersion relation of the Q2D plasmons ω_p^{+} and ω_p^{10} of the asymmetric truncated DPQW calculated self-consistently in RPA in dependence on the wave vector component $q_\parallel$ for $n_{2DEG}=1\times 10^{11}$ cm^{-2}. The hatched areas correspond to the single-particle continua.

7(c), and 8(c) for the ground state] are depicted in Figs. 16 and 17. As seen from Fig. 16 the ISC results in a resonance splitting (anticrossing) of the modes ω_p^{+} and ω_p^{10}. Here, we keep the denotation ω_p^{+} and ω_p^{10} for comparison with the dispersion curves of the two other DPQW's under consideration. The resonance splitting is $\omega_p^{10}-\omega_p^{00}\approx 1\times 10^{11}$ s^{-1}. The both independent branches ω_p^{+} and ω_p^{10} of a symmetric truncated DPQW become hybrid-type modes (coupled or mixed modes) in the anticrossing range. For small wave vectors the lower-frequency branch behaves like ω_p^{+} and the higher-frequency branch like ω_p^{10}. The opposite is valid for larger wave vectors. The dispersion curves of the higher-frequency intersubband plasmons are plotted in Figs. 17(a) and 17(b) for two different electron densities. The general feature of the dispersion curves is very similar to that of the symmetric truncated DPQW [cf. Figs. 15(a) and 15(b)]. But in difference to the symmetric truncated DPQW the ISC between the collective intersubband transitions $1\leftrightarrow 2$ and $0\leftrightarrow 2$ on the one hand and $1\leftrightarrow 3$ and $0\leftrightarrow 3$ on the other hand leads to a repelling of the mode ω_p^{21} from ω_p^{20} and of ω_p^{31} from ω_p^{30}. Thus, the separation between these branches increases with increasing asymmetry of the bare confining potential. It is important to note that for the larger electron density the dispersion curve of the branch ω_p^{21} is in the very near vicinity of the upper boundary ω_1^{20} of the single-particle $(2-0)$ intersubband continuum with a stop-point at $q_\parallel\approx 2\times 10^{3}$ cm^{-1}, not to be drawn in Fig. 17(b).

V. OPTICAL PROPERTIES

In this section we consider the optical properties of SPQW's and DPQW's. In particular, we examine the optical transmission spectra in the presence of a grating coupler on top of the samples. The grating is necessary because in far-infrared (FIR) transmission spectroscopy the investigation of the mode dispersion is not directly accessible. A grating with periodicity d modulates the incident radiation [with in-plane wave vector $\mathbf{k}_\parallel=(k_x,k_y)$] and induces electromagnetic field components of wave vectors $k_{\parallel n}=(k_x+G_n,k_y)$, where $G_n=(2\pi/d)n$; $n=0,\pm 1,\pm 2,\ldots$. Thus, the incident light is coupled via the action of the grating coupler to the Q2D plasmons and it is possible to study the Q2D plasmon dispersion relation $\omega_p^{Q2D}(\mathbf{q}_\parallel)$ as a function of the wave vector $\mathbf{q}_\parallel=\mathbf{k}_{\parallel n}=(k_{xn},k_y)$, where $k_{xn}=k_x+G_n$ and $k_x=(\omega/c)\sin\Theta_0$ (Θ_0: ray angle of the incident light measured from the z axis) is the wave vector component of the incident light beam perpendicular to the stripes forming the grating, which are parallel to the y direction. Our calculation of the optical transmission spectra follows the method developed in Ref. 31, which is applicable for all layered systems with grating including the optical anisotropy of that layer which contains the Q2DEG. This method is based on the transfer-matrix method of local optics and the modal-expansion method to include the influence of the grating. It is

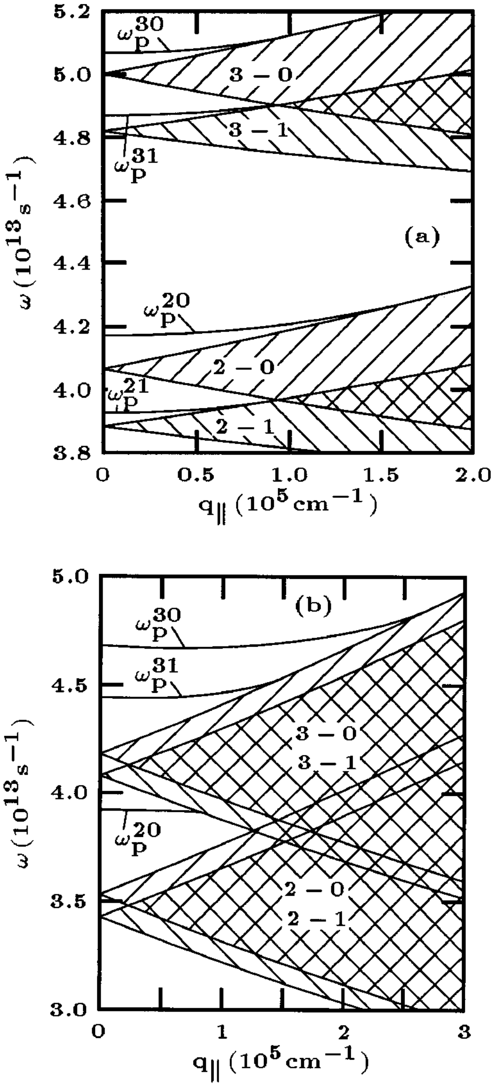

FIG. 17. Dispersion relation of the Q2D plasmons ω_p^{21}, ω_p^{20}, ω_p^{31}, and ω_p^{30} of the asymmetric truncated DPQW calculated self-consistently in RPA in dependence on the wave vector component $q_\parallel$ for $n_{2DEG}=1\times10^{11}$ cm^{-2} (a) and for $n_{2DEG}=5\times10^{11}$ cm^{-2} (b). The hatched areas correspond to the single-particle continua.

shown that the combination of both methods results in a generally computationally efficient and stable formalism of the optical response of multilayer systems filled by isotropic and anisotropic media with grating.[31] As shown in Ref. 31 the use of local optics provides an excellent approximation to describe the long-wavelength response of the Q2DEG as long as the size quantization is incorporated in the theory.

To model the QW structures considered in this paper we use a four-layer system: $\nu=1,\ldots,4$. Each layer is, in general, characterized by its thickness $d_\nu=|z_\nu-z_{\nu-1}|$ and by its local dielectric tensor $\varepsilon^{(\nu)}_{\alpha\beta}(\mathbf{x},\omega)$, where $\alpha,\beta=x,y,z$. Here, z_ν is the position of the interface between the νth and $(\nu+1)$th layer. Note, that the parameters used here z_ν of the layer system are not identical to the parameters $z_1,\ldots,z_4$ used by the calculation of the ground-state properties of the Q2DEG in Sec. II. Here, we use the parameters for the whole sample, because we want to describe the optical properties of the whole structure, modeled as a multilayer system with grating, whereas in Sec. II only the media in the near vicinity of the QW's have a perceptible influence on the ground-state properties of the Q2DEG. The media $\nu=0$ and $\nu=5$, above and below the multilayer system, are assumed to be filled by vacuum with $\varepsilon_0(\omega)=\varepsilon_5(\omega)=1$. The layer $z_1<z<z_0$ contains the rectangular-groove grating of height $h\equiv d_1$, periodicity $d=a+b$ and mark-to-space ratio $t=a/b$. In the grating region we have $\varepsilon_{\alpha\beta}(\mathbf{x},\omega)=\varepsilon_\xi(\omega)\delta_{\alpha\beta}$, where $\xi=a$ if $md<x<md+a$ and $\xi=b$ if $md+a<x<(m+1)d$; $m=0,\pm1,\pm2,\ldots$. Here, we assume a silver grating, described by $\varepsilon_a(\omega)=1-\omega_p^2/[\omega(\omega+i\gamma)]$ for the filled stripes, where $\omega_p=5.69\times10^{15}$ s^{-1} is the plasma frequency and $\gamma=7.596\times10^{13}$ s^{-1} is the phenomenological damping constant, and for the spacing between the stripes we assume $\varepsilon_b=1$. The semiconductor layers $\nu=2$ and $\nu=4$, $z_2<z<z_1$ and $z_4<z<z_3$, respectively, are filled by Ga$_{1-x}$Al$_x$As, described in the framework of the ε_s-approximation by $\varepsilon_{s2}=\varepsilon_{s4}=12.21$, assuming $x=0.25$. The layer $\nu=3$, $z_3<z<z_2$ forming the SPQW or the DPQW, i.e., which contains the Q2DEG, is described by the local dielectric tensor $\varepsilon^{(3)}_{\alpha\beta}(\omega)$: $\varepsilon^{(3)}_{xx}(\omega)=\varepsilon^{(3)}_{yy}(\omega)\neq0$, $\varepsilon^{(3)}_{zz}(\omega)\neq0$, but $\varepsilon^{(3)}_{xy}(\omega)=\varepsilon^{(3)}_{yx}(\omega)=\varepsilon^{(3)}_{xz}(\omega)=\varepsilon^{(3)}_{zx}(\omega)=\varepsilon^{(3)}_{yz}(\omega)=\varepsilon^{(3)}_{zy}(\omega)=0$. The layer $\nu=3$ is identical to the region of the SPQW and of the DPQW with a thickness of $d_3=a_{2DEG}$, where a_{2DEG} is the effective thickness of the Q2DEG described below, while d_2 and d_4 are not necessarily equal to l_d+l_s. This four-layer system is schematically drawn in the inset of Fig. 18. The nonvanishing components of the macroscopic local dielectric tensor are given for a QW, described by a two-subband model assuming that only the lowest subband is occupied, by[10]

$$\varepsilon^{(3)}_{xx}(\omega)=\varepsilon^{(3)}_{yy}(\omega)=\varepsilon_{s3}\left(1-\frac{\omega_0^2}{\omega\left(\omega+\dfrac{i}{\tau_\parallel}\right)}\right), \tag{46}$$

$$\varepsilon^{(3)}_{zz}(\omega)=\varepsilon_{s3}\left(1-\frac{\omega_0^2 f_{10}}{\omega^2-\Omega_{10}^2+\dfrac{i}{\tau_\perp}\omega}\right). \tag{47}$$

Herein, we have defined the plasma frequency by $\omega_0=[n_{2DEG}e^2/(m_e\varepsilon_0\varepsilon_{s3}a_{2DEG})]^{1/2}$, where a_{2DEG} is the effective layer thickness of the Q2DEG and $\tau_\parallel$, $\tau_\perp$ are the phenomenological longitudinal and transverse relaxation times, respectively. Further, f_{10} is the oscillator strength, given in Appendix A. In the case of a four-subband model one obtains (see Appendix A):

$$\varepsilon^{(3)}_{xx}(\omega)=\varepsilon^{(3)}_{yy}(\omega)=\varepsilon_{s3}\left(1-\frac{\omega_0^2}{\omega\left(\omega+\dfrac{i}{\tau_\parallel}\right)}\right), \tag{48}$$

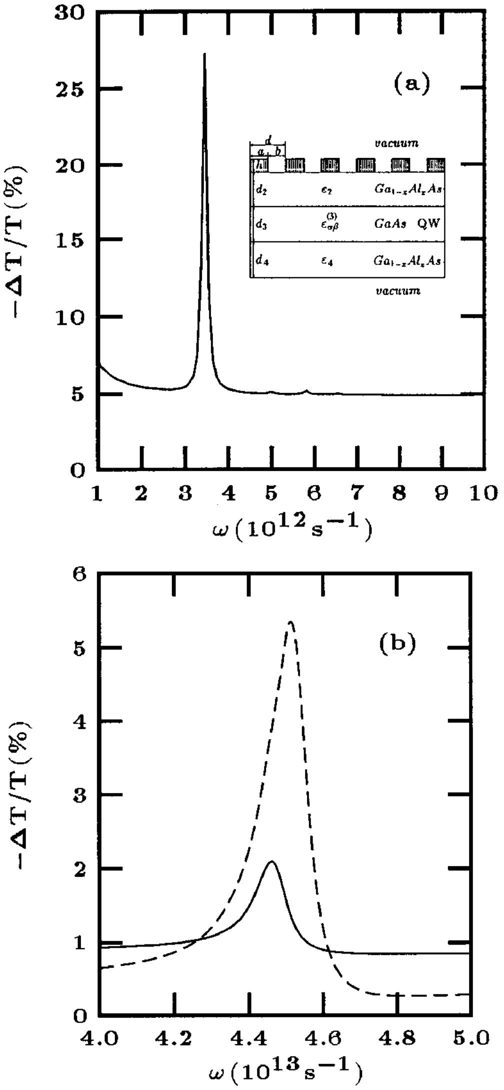

FIG. 18. Calculated relative change in the optical transmission in the frequency range of the intrasubband plasmon ω_p^{00} (a) and in the frequency range of the intersubband plasmon ω_p^{10} (b) of the SPQW.

$$\varepsilon_{zz}^{(3)}(\omega)=\varepsilon_{s3}\left(1-\frac{\omega_0^2 f_{10}}{\omega^2-\Omega_{10}^2+\dfrac{i}{\tau_\perp}\omega}-\sum_{K=2}^{3}\left[\frac{(\omega_0^{(0)})^2 f_{K0}}{\omega^2-\Omega_{K0}^2+\dfrac{i}{\tau_\perp}\omega}+\frac{(\omega_0^{(1)})^2 f_{K1}}{\omega^2-\Omega_{K1}^2+\dfrac{i}{\tau_\perp}\omega}\right]\right), \tag{49}$$

where $f_{KK'}$ is given in Appendix A. It is important to note that for mirror-symmetric QW's $f_{KK'}=0$ if $K+K'=$even number. Further, we have defined $\omega_0^{(0)}=[N_0 e^2/(m_e\varepsilon_0\varepsilon_{s3}a_{2DEG})]^{1/2}$ and $\omega_0^{(1)}=[N_1 e^2/(m_e\varepsilon_0\varepsilon_{s3}a_{2DEG})]^{1/2}$. The parameters used in the numerical calculation are $\varepsilon_{s3}=12.87$, corresponding to ε_s of GaAs, $\tau_\parallel=1\times 10^{-11}$ s and $\tau_\perp=1\times 10^{-12}$ s.

The quantity which is usually extracted from FIR transmission experiments is the relative change in the transmission $\Delta T/T=1-T(Y)/T(X)$, where T is the power transmission coefficient depending on X and Y. Here, we use $X=n_{2DEG}$ and $Y=0$. Further, we assume that only the zeroth-order diffracted wave is a propagating wave above and below the sample, i.e., $k_{zn}^{(0)}=[\omega^2/c^2-(\omega/c\sin\Theta_0+2\pi n/d)^2]^{1/2}$ is real and positive for $n=0$, but all higher-order diffracted waves $(n=\pm 1,\pm 2,\dots)$ are assumed to be evanescent and thus, not propagating in the z direction, i.e., its z component of the wave vector $k_{zn}^{(0)}$ is pure imaginary. This is the usual situation realized in experiments. The case that higher-order diffracted waves become propagating, e.g., by increasing the period of the grating, is not considered in this paper. The reader who is interested in this question, i.e., in the occurrence of Wood anomalies or more specifics of Rayleigh anomalies, is directed to Refs. 31 and 32. For the numerical calculations we have used the following parameters for the grating: $h=10$ nm, $d=1$ μm, and $t=0.5$ and for the layer thicknesses: $d_2=0.1$ μm, $d_4=1$ μm, and $d_3=a_{2DEG}$ is the effective thickness of the considered QW (see Appendix A). Further, we assume perpendicularly incident light $(\Theta_0=0°)$.

The relative transmission $-\Delta T/T$ of the semiconductor sample containing the SPQW under consideration is plotted in Fig. 18(a) in the frequency range of the intrasubband plasmon ω_p^{00}. The largest peak in the $-\Delta T/T$ spectrum results from the excitation of the intrasubband plasmon at $q_\parallel=k_{x1}=6.28\times 10^4$ cm^{-1}. The small minima at higher frequencies result from the excitation of intrasubband plasmons with higher wave vectors $q_\parallel=k_{xn}$: $k_{x2}=1.256\times 10^5$ cm^{-1}, $k_{x3}=1.885\times 10^5$ cm^{-1}, and $k_{x4}=2.513\times 10^5$ cm^{-1}. The relative transmission spectra are plotted in the frequency range of the intersubband plasmon ω_p^{10} in Fig. 18(b) for two different electron densities. Because $-\Delta T/T$ is calculated in the framework of local optics, the intersubband plasmon excited at $q_\parallel=k_{xw}$, $|n|\geqslant 1$ is dispersionless and thus, peaks at frequencies different from $\omega_p^{10}(q_\parallel=0)$ are absent in the plotted spectra. It is seen that this peak occurs at nearly the same frequency for both electron densities as a result of Kohn's theorem (see discussion in Sec. IV A). Thus, we obtain that the generalized Kohn's theorem is relatively insensitive (or stable) to the used approximations: finite height of the parabolic well which is terminated by square barriers, approximations made performing the numerical calculations and the use of simple local optics. Similar results for the optical properties of SPQW's were found in Refs. 23 and 33, where the optical absorption in the absence of a grating coupler is calculated. It is important to note that in the absence of a grating coupler normally incident light cannot excite a normal mode neither Q2D intra nor intersubband plasmons. This is true, because the wave vector of the intrasubband plasmon is always larger than the wave vector of light, propagating in a media with the background dielectric constant ε_s. This is also true for the Q2D intersubband plasmon because the nonradiative normal modes lie to the right of the light line. Due to the polariton effect the collective intersubband transition is accompanied by a radiative virtual mode with a branch appearing to the left of the light line. To excite this radiative intersubband plasmon a z component of the external electric field is necessary, which is equal to zero in the case of normally incident light. In the case with grating coupler, there

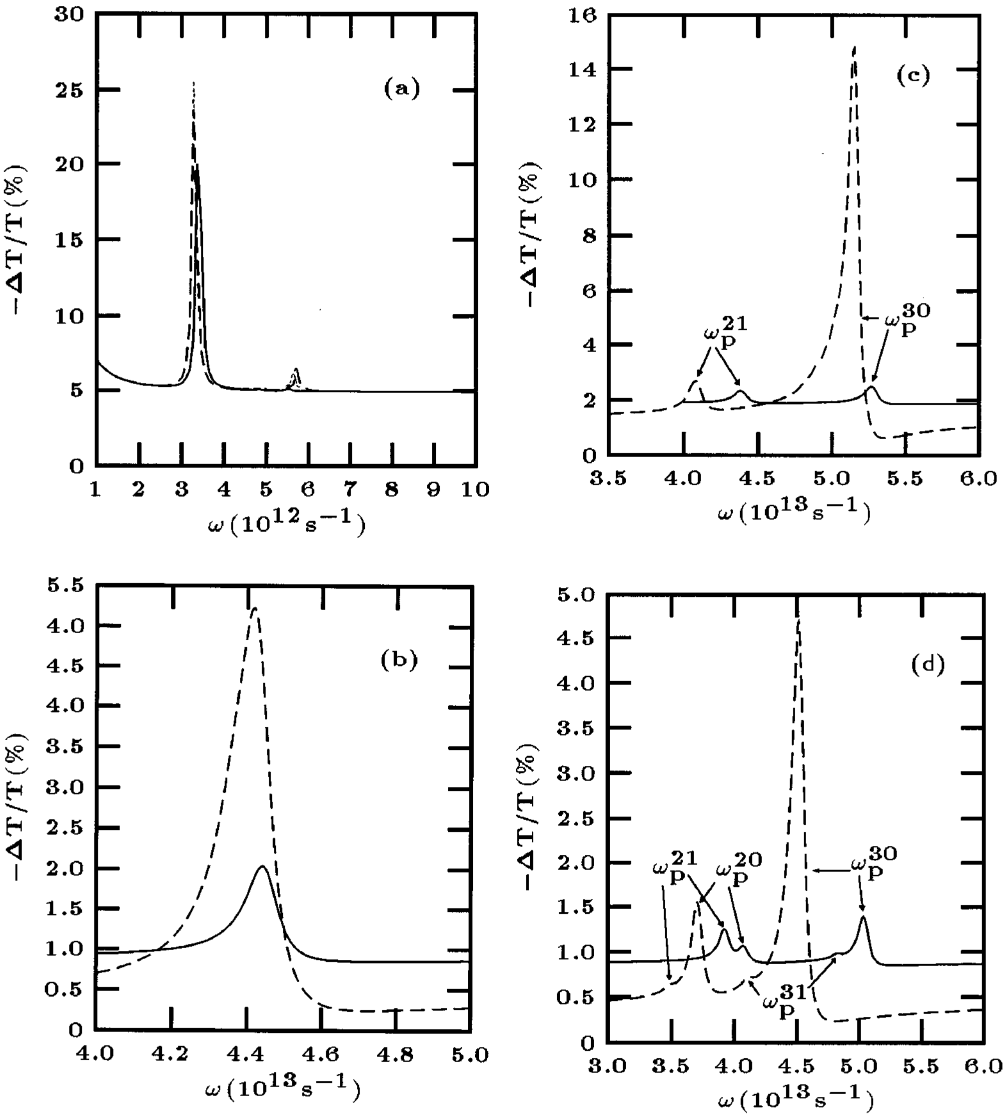

FIG. 19. Calculated relative change in the optical transmission in the frequency range of the intrasubband plasmon ω_p^+ and the intersubband plasmon ω_p^{10} (a) for the symmetric DPQW (solid line), for the symmetric truncated DPQW (dashed line), and for the asymmetric truncated DPQW (dotted line); and in the frequency range of the higher-frequency intersubband plasmons of the symmetric DPQW (b), of the symmetric truncated DPQW (c), and of the asymmetric truncated DPQW (d).

always exists a nonvanishing z component of the electric field, which is connected with the higher-order diffracted waves with k_{xn}, $|n|\geqslant 1$ and so it is possible to excite both the radiative and the nonradiative intersubband plasmon at wave vectors $q_\parallel = k_{xn}$, $|n|\geqslant 1$. The height of the peak in Fig. 18(b) increases with increasing electron density because the oscillator strength f_{10} as well as ω_0 increase in this case. We obtain $f_{10}=1.08424$ and $\omega_0=1.52\times 10^{13}$ s^{-1} for $n_{2DEG}=1\times 10^{11}$ cm^{-2} and $f_{10}=1.08545$ and $\omega_0 = 3.19\times 10^{13}$ s^{-1} for $n_{2DEG}=5\times 10^{11}$ cm^{-2}. Because of the approximations made $f_{KK'}$ is no more a true oscillator strength fulfulling the f-sum rule. It is noticeable that the position of the maximum agrees very well with $\omega_p^{10}(q_\parallel=0)$. This is true because for the considered model the ISC between ω_p^{00} and ω_p^{10} is zero and thus, the local macroscopic dielectric tensor, in which intra- and intersubband processes are decoupled, is suitable to describe the dynamical response of the Q2DEG.

In Fig. 19(a) we present the relative transmission $-\Delta T/T$ of semiconductor samples containing the symmetric DPQW, the symmetric truncated DPQW and the asymmetric truncated DPQW. The peaks associated with the excitation of the intrasubband plasmon ω_p^+ at $q_\parallel = k_{x1}$ dominate the spectra for the three different DPQW's. The peaks resulting from the excitation of ω_p^+ at higher wave vector components at $\omega\approx 4.8\times 10^{12}$ s^{-1} and at $\omega\approx 5.5\times 10^{12}$ s^{-1} and that resulting from the excitations of the lowest-frequency intersubband plasmon ω_p^{10} at $\omega\approx 5.7\times 10^{12}$ s^{-1} (occur only in the case of the symmetric and asymmetric truncated DPQW's) are very small in magnitude.

Figures 19(b)–19(d) show the relative transmission spectra of the symmetric DPQW (b), the symmetric truncated DPQW (c) and of the asymmetric truncated DPQW (d) in the frequency range of the higher-frequency intersubband plasmons. The peak in Fig. 19(b) corresponds to the excitation of

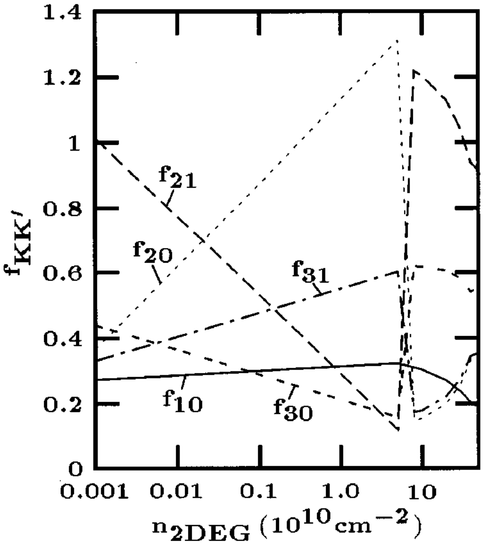

FIG. 20. Oscillator strength of the intersubband plasmons of the asymmetric truncated DPQW in dependence on the electron number density.

the intersubband plasmon ω_p^{30} at $q_\parallel = k_{x1}$. This is true because the symmetric modes ω_p^{20} and ω_p^{31} are not dipole-active ($f_{20} = f_{31} = 0$) and ω_p^{21} has a very small oscillator strength $f_{21} = 1.26 \times 10^{-3}$ compared to $f_{30} = 1.08$ at $n_{2DEG} = 1 \times 10^{11}$ cm^{-2}. An increasing electron density increases the peak height and slightly shifts its position.

From Fig. 19(c) it becomes obvious that for the symmetric truncated DPQW the oscillator strength of the mode ω_p^{21} increases so that it becomes observable in the $-\Delta T/T$ spectrum. It is seen that the oscillator strength f_{10} increases more rapidly with increasing electron density than f_{21}. Thus, as dipole selection rule for FIR optical transmission spectroscopy on symmetric and symmetric truncated DPQW's we obtain that only intra- and antisymmetric intersubband plasmons absorb FIR light.

The corresponding relative transmission spectrum of the sample with the asymmetric truncated DPQW is plotted in the frequency range of the higher-frequency intersubband plasmons in Fig. 19(d). In this case all intersubband plasmons, ω_p^{21}, ω_p^{20}, ω_p^{31}, and ω_p^{30}, can be excited by FIR radiation. But it is seen that the peaks associated with the excitation of ω_p^{21} and ω_p^{30} have a much larger magnitude than those of ω_p^{20} and ω_p^{31}. With increasing electron density the peak height at the positions of ω_p^{20} and ω_p^{30} is larger than that of ω_p^{21} and ω_p^{31}. In Fig. 20 the oscillator strengths $f_{KK'}$ of the higher-frequency intersubband plasmons are plotted in dependence on the electron density of the Q2DEG. From this figure it becomes obvious that the modes ω_p^{21} and ω_p^{20} "exchange" oscillator strength: the oscillator strength f_{21} increases while f_{20} decreases with increasing electron density up to $n_{2DEG} \approx 0.8 \times 10^{11}$ cm^{-2} and the opposite is valid above this density. This is a typical effect induced by the ISC. Such an exchange of oscillator strength in dependence on the gate voltage, which effectively changes the electron concentration, was observed by Hartung *et al.*[27] in FIR transmission spectroscopy on asymmetric coupled quantum wells, i.e., in a very similar situation as the here considered. It is seen that the use of local optics provides reasonable results for the relative transmission when using the dielectric tensor including size quantization and ISC between the intersubband modes. This is true as long as the LWA for the dispersion relation is a satisfactory approximation.

For the asymmetric truncated DPQW the absolute values of the peak positions do not very well agree with those of the modes, calculated from the dispersion relation. This is true because for the DPQW's the effective thickness a_{2DEG} used in the numerical calculations is not a very well defined quantity. But nevertheless, the theoretical calculated relative transmission spectra give all qualitative features in an excellent way and the quantitative results are in a good approximation even for DPQW's with two occupied subbands, where ISC effects become important.

VI. SUMMARY

In this paper we have investigated the dynamical response of double parabolically graded quantum wells, both symmetric and asymmetric coupled parabolic quantum wells, to examine: (i) the Q2D plasmons and (ii) the optical properties. In the framework of the random-phase approximation a fully self-consistent procedure is employed to calculate the ground state and the dynamical response.

We have shown that for double parabolically graded quantum wells with a narrow barrier, so that tunneling is possible, strong intersubband coupling results in a hybrid-type mode spectrum. Applying a four-subband model with the two lowest-lying subbands to be occupied, we find that the collective intrasubband motion has two branches. It is shown that only the higher-frequency branch is observable because the lower-frequency branch appears strongly Landau damped in the single-particle intrasubband continuum. This is quite different from the intrasubband plasmons of a Q1DEG, where both intrasubband plasmon branches are observable and free of Landau damping.[34–36] As long as the two parabolic quantum wells are symmetric coupled, the lowest-frequency intersubband mode crosses the dispersion curve of the upper intrasubband mode. Breaking this symmetry, anticrossing of the dispersion curves and thus resonance splitting occurs which is a result of the intersubband-coupling effect.

In the framework of a four-subband model with two occupied subbands, four higher-frequency intersubband plasmon modes result. These modes are associated with the collective intersubband motion $1 \leftrightarrow 2$, $0 \leftrightarrow 2$, $1 \leftrightarrow 3$, and $0 \leftrightarrow 3$. The frequencies of these branches occur as doublets for thicker barriers, which become degenerate if tunneling is suppressed. In this case the collective electron motion in the two separated quantum wells is coupled only via the Coulomb coupling between the oscillating charges. With decreasing barrier thickness the splitting of both doublets increases and the intersubband coupling decreases too. Further, an increasing electron density reduces the splitting of both doublets. This results because Coulomb repulsion of the electrons in both quantum wells increases with increasing electron density. This effectively increases the separation of the two quantum wells.

Regarding the optical properties of coupled parabolic quantum wells, we find as the dipole selection rule that as long as the quantum systems are spatial symmetric only the upper branch of the intrasubband plasmons and the antisymmetric intersubband plasmons are dipole active and thus appear in the transmission spectra. Breaking this symmetry all plasmon modes appear in the transmission spectrum. Varying the electron density, this results in an exchange of oscillator strength between the modes due to the intersubband coupling.

ACKNOWLEDGMENTS

The authors gratefully acknowledge financial support of the Deutsche Forschungsgemeinschaft (DFG), Project No. We 1532/3-2.

APPENDIX: MACROSCOPIC DIELECTRIC TENSOR

The nonlocal RPA dielectric tensor of a Q2DEG is calculated in Ref. 10 to be

$$\varepsilon_{\alpha\beta}(\mathbf{x},\mathbf{x}'|\omega)=\varepsilon_s(\mathbf{x})\,\delta(\mathbf{x}-\mathbf{x}')\,\delta_{\alpha\beta}-\frac{1}{\varepsilon_0\omega^2}P_{\alpha\beta}(\mathbf{x},\mathbf{x}'|\omega), \tag{A1}$$

where the RPA polarization tensor $P_{\alpha\beta}(\mathbf{x},\mathbf{x}'|\omega)$ is given by

$$P_{\alpha\beta}(\mathbf{x},\mathbf{x}'|\omega)=\frac{1}{A}\sum_{\mathbf{q}_\parallel} e^{i\mathbf{q}_\parallel\cdot(\mathbf{x}_\parallel-\mathbf{x}'_\parallel)}P_{\alpha\beta}(\mathbf{q}_\parallel;z,z'|\omega), \tag{A2}$$

$$\begin{aligned}P_{\alpha\beta}(\mathbf{q}_\parallel;z,z'|\omega)&=\sum_{KK'}P_{\alpha\beta}^{KK'}(\mathbf{q}_\parallel,\omega)\,\xi_\alpha^{KK'}(z)\,\xi_\beta^{KK'}(z')^*\\&=P_{\beta\alpha}^*(\mathbf{q}_\parallel;z,z'|\omega)\end{aligned} \tag{A3}$$

with

$$\begin{aligned}P_{xx}^{KK'}(\mathbf{q}_\parallel,\omega)=-\sum_{\mathbf{k}_\parallel}\Bigg(&\frac{\hbar^2e^2}{4m_e^2}P_{KK'}^{(1)}(\mathbf{q}_\parallel,\mathbf{k}_\parallel|\omega)(2k_\parallel\cos\varphi+q_\parallel)^2\\&+\frac{2e^2}{m_eA}n_F(\mathcal{E}_K(\mathbf{k}_\parallel))\Bigg),\end{aligned} \tag{A4}$$

$$\begin{aligned}P_{xz}^{KK'}(\mathbf{q}_\parallel,\omega)&=i\sum_{\mathbf{k}_\parallel}\frac{\hbar^2e^2}{4m_e^2}P_{KK'}^{(1)}(\mathbf{q}_\parallel,\mathbf{k}_\parallel|\omega)(2k_\parallel\cos\varphi+q_\parallel)\\&=-P_{zx}^{KK'}(\mathbf{q}_\parallel,\omega),\end{aligned} \tag{A5}$$

$$\begin{aligned}P_{yy}^{KK'}(\mathbf{q}_\parallel,\omega)=-\sum_{\mathbf{k}_\parallel}\Bigg(&\frac{\hbar^2e^2}{4m_e^2}P_{KK'}^{(1)}(\mathbf{q}_\parallel,\mathbf{k}_\parallel|\omega)(2k_\parallel\sin\varphi)^2\\&+\frac{2e^2}{m_eA}n_F(\mathcal{E}_K(\mathbf{k}_\parallel))\Bigg),\end{aligned} \tag{A6}$$

$$\begin{aligned}P_{zz}^{KK'}(\mathbf{q}_\parallel,\omega)=-\sum_{\mathbf{k}_\parallel}\Bigg(&\frac{\hbar^2e^2}{4m_e^2}P_{KK'}^{(1)}(\mathbf{q}_\parallel,\mathbf{k}_\parallel|\omega)\\&+\frac{e^2\hbar}{m_e^2A\Omega_{KK'}}n_F(\mathcal{E}_K(\mathbf{k}_\parallel))\Bigg).\end{aligned} \tag{A7}$$

Herein is

$$\xi_\alpha^{KK'}(z)=(1-\delta_{\alpha z})\,\eta_{KK'}(z)+\delta_{\alpha z}g_{KK'}(z) \tag{A8}$$

and

$$g_{KK'}(z)=\varphi_K(z)\frac{d}{dz}\varphi_{K'}^*(z)-\varphi_{K'}^*(z)\frac{d}{dz}\varphi_K(z). \tag{A9}$$

The wavelength of the incident FIR light (external field) is large compared to the effective thickness a_{2DEG} of the Q2DEG so that we can consider the dynamical properties in the optical limit $q_\parallel\to0$: $P_{\alpha\beta}(0;z,z'|\omega)$. Further, this makes it possible to average the physical quantities over the effective layer thickness. For the induced current it follows $\mathbf{j}^{opt}=1/a_{2DEG}\int_0^{a_{2DEG}}dz\,\mathbf{j}^{ind}$:

$$\begin{aligned}j_\alpha^{opt}(\mathbf{q}_\parallel;z|\omega)=\sum_\beta A_\beta^{opt}(\mathbf{q}_\parallel;z|\omega)&\frac{1}{a_{2DEG}}\int_0^{a_{2DEG}}dz\\&\times\int_0^{a_{2DEG}}dz'\,P_{\alpha\beta}(0;z,z'|\omega).\end{aligned} \tag{A10}$$

Equation (A10) is an approximation because it is assumed that the total vector potential varies only slowly over a_{2DEG}. This is strictly true only for the external field. Because $\mathbf{A}=\mathbf{A}^{ext}+\mathbf{A}^{ind}$ we neglect the rapid fluctuations in $\mathbf{A}^{ind}$. From Eq. (A10) it follows the optical, i.e., macroscopic polarization tensor

$$P_{\alpha\beta}^{opt}(\omega)=\frac{1}{a_{2DEG}}\int_0^{a_{2DEG}}dz\int_0^{a_{2DEG}}dz'\,P_{\alpha\beta}(0;z,z'|\omega). \tag{A11}$$

Using Eqs. (A3)–(A7) in (A11) it follows

$$P_{xx}^{opt}(\omega)=P_{yy}^{opt}(\omega)=-\frac{e^2}{m_ea_{2DEG}}\sum_K N_K, \tag{A12}$$

$$P_{zz}^{opt}(\omega)=-\frac{e^2\omega^2}{m_ea_{2DEG}}\sum_{K=1}^{\infty}\sum_{K'<K}\frac{2m_e\Omega_{KK'}}{\hbar}\,\frac{N_K+N_{K'}}{\omega^2-\Omega_{KK'}^2}\,z_{KK'}^2, \tag{A13}$$

where

$$z_{KK'}=\int_0^{a_{2DEG}}dz\,z\,\eta_{KK'}(z). \tag{A14}$$

It becomes obvious that the averaging decouples intra- and intersubband transitions. But all the possible collective intrasubband transitions are coupled as well as all the possible collective intersubband transitions. If the confining potential is symmetric, $z_{KK'}=0$ if $K+K'=$ even number. Then, for a QW assuming a two-subband model with one occupied subband it follows that

$$\varepsilon_{xx}^{opt}(\omega)=\varepsilon_{yy}^{opt}(\omega)=\varepsilon_s\left(1-\frac{\omega_0^2}{\omega\left(\omega+\dfrac{i}{\tau_\parallel}\right)}\right), \tag{A15}$$

$$\varepsilon_{zz}^{opt}(\omega)=\varepsilon_s\left(1-\frac{\omega_0^2f_{10}}{\omega^2-\Omega_{10}^2+\dfrac{i}{\tau_\perp}\omega}\right), \tag{A16}$$

where

$$f_{10}=\frac{2m_e\Omega_{10}}{\hbar}z_{10}^2 \tag{A17}$$

is the oscillator strength of the collective intersubband transition $0 \rightarrow 1$ and $\omega_0^2 = n_{2DEG} e^2 / (m_e \varepsilon_0 \varepsilon_s a_{2DEG})$ is the plasma frequency. Here, we have introduced the phenomenological longitudinal and transverse relaxation times $\tau_\parallel$ and $\tau_\perp$, respectively. The results (A15) and (A16) are valid for all SQW's independent from the potential shape. The dependence of $\varepsilon_{\alpha\beta}^{opt}(\omega)$ from the potential shape of the QW is via $z_{KK'}$ only. Similar results were given in Refs. 4 and 37.

For a QW assuming a four-subband model with two occupied subbands we obtain from Eq. (A11)

$$\varepsilon_{xx}^{opt}(\omega) = \varepsilon_{yy}^{opt}(\omega) = \varepsilon_s \left(1 - \frac{\omega_0^2}{\omega \left(\omega + \frac{i}{\tau_\parallel} \right)} \right), \tag{A18}$$

$$\varepsilon_{zz}^{opt}(\omega) = \varepsilon_s \left(1 - \frac{\omega_0^2 f_{10}}{\omega^2 - \Omega_{10}^2 + \frac{i}{\tau_\perp}\omega} - \sum_{K=2}^{3} \left[\frac{(\omega_0^{(0)})^2 f_{K0}}{\omega^2 - \Omega_{K0}^2 + \frac{i}{\tau_\perp}\omega} + \frac{(\omega_0^{(1)})^2 f_{K1}}{\omega^2 - \Omega_{K1}^2 + \frac{i}{\tau_\perp}\omega} \right] \right), \tag{A19}$$

where

$$f_{KK'} = \frac{2 m_e \Omega_{KK'}}{\hbar} z_{KK'}^2 \tag{A20}$$

is the oscillator strength of the collective intersubband transition $K' \rightarrow K$ and $(\omega_0^{(0)})^2 = N_0 e^2/(m_e \varepsilon_0 \varepsilon_s a_{2DEG})$, $(\omega_0^{(1)})^2 = N_1 e^2/(m_e \varepsilon_0 \varepsilon_s a_{2DEG})$. Please note that for symmetric confining potentials $f_{KK'} = 0$ if $K + K'$ $=$ even number.

The effective thickness a_{2DEG} of the QW is a parameter, which cannot be determined directly by the average procedure itself described above. In the case of a two-subband model with one occupied subband, as one suitable possibility, we determine a_{2DEG} in such a way that the zero of $\varepsilon_{zz}^{opt}(\omega)$ corresponds to $\omega_p^{10}(q_\parallel = 0)$. The result is $a_{2DEG} = 2 z_{10}^2 / \alpha_{1010}$, where the matrix element α_{1010} is given by $\alpha_{KK'KK'} = \int_0^{a_{2DEG}} dz \int_0^{a_{2DEG}} dz' \, \eta_{KK'}(z) |z - z'| \, \eta_{KK'}(z')$. In the case of a four-subband model with two occupied subbands the determination of a_{2DEG} in the above described way is not possible. In this case we use $a_{2DEG} = \mathrm{Max}[a_{2DEG}^{KK'KK'}]$, where $a_{2DEG}^{KK'KK'} = 2 z_{KK'}^2 / \alpha_{KK'KK'}$.

---

[1] T. Ando, A. B. Fowler, and F. Stern, Rev. Mod. Phys. **54**, 437 (1982).

[2] F. Stern, Phys. Rev. Lett. **18**, 546 (1967).

[3] A. V. Chaplik, Zh. Eksp. Teor. Fiz. **62**, 746 (1972) [Sov. Phys. JETP **35**, 395 (1972)].

[4] D. Dahl and L. J. Sham, Phys. Rev. B **16**, 651 (1977).

[5] A. C. Tselis and J. J. Quinn, Surf. Sci. **113**, 362 (1982).

[6] L. Wendler and R. Pechstedt, Phys. Status Solidi B **138**, 197 (1986).

[7] L. Wendler and R. Pechstedt, Phys. Rev. B **35**, 5887 (1987).

[8] L. Wendler and R. Pechstedt, Phys. Status Solidi B **141**, 129 (1987).

[9] L. Wendler, R. Haupt, and V. G. Grigoryan, Physica B **167**, 91 (1990); **167**, 101 (1990); **167**, 113 (1990).

[10] L. Wendler and E. Kändler, Phys. Status Solidi B **177**, 9 (1993).

[11] S. J. Allen, Jr., D. C. Tsui, and R. A. Logan, Phys. Rev. Lett. **38**, 980 (1977).

[12] T. N. Theis, J. P. Kotthaus, and P. J. Stiles, Solid State Commun. **35**, 875 (1980).

[13] E. Batke, D. Heitmann, and C. W. Tu, Phys. Rev. B **34**, 6951 (1986).

[14] D. Olego, A. Pinczuk, A. Gossard, and W. Wiegemann, Phys. Rev. B **25**, 7867 (1982).

[15] R. Sooryakumar, A. Pinczuk, A. C. Gossard, and W. Wiegemann, Phys. Rev. B **31**, 2578 (1985).

[16] D. Heitmann, Surf. Sci. **170**, 332 (1986).

[17] E. Batke, Adv. Solid State Phys. **31**, 297 (1991).

[18] A. Wixforth, Semicond. Sci. Technol. **9**, 215 (1994).

[19] L. Wendler and V. G. Grigoryan, Solid State Commun. **71**, 527 (1989).

[20] S. Ernst, A. R. Goñi, K. Syassen, and K. Eberl, Phys. Rev. Lett. **72**, 4029 (1994).

[21] P. Ruden and G. H. Döhler, Phys. Rev. B **27**, 3547 (1983).

[22] L. Brey, N. F. Johnson, and B. I. Halperin, Phys. Rev. B **40**, 10 647 (1989).

[23] L. Brey, J. Dempsey, N. F. Johnson, and B. I. Halperin, Phys. Rev. B **42**, 1240 (1990).

[24] S. Das Sarma and A. Madhukar, Phys. Rev. B **23**, 805 (1981).

[25] S. Das Sarma and P. I. Tamborenea, Phys. Rev. Lett. **73**, 1971 (1994).

[26] R. Decca, A. Pinczuk, S. Das Sarma, B. S. Dennis, L. N. Pfeiffer, and K. W. West, Phys. Rev. Lett. **72**, 1506 (1994).

[27] M. Hartung, A. Berger, A. Wixforth, P. F. Hopkins, J. H. English, and A. C. Gossard, in *22nd International Conference on The Physics of Semiconductors*, edited by D. J. Lockwood (World Scientific, Singapore, 1995), p. 1087.

[28] F. Stern and S. Das Sarma, Phys. Rev. B **30**, 840 (1984).

[29] G. A. M. Hurkx and W. van Haeringen, J. Phys. C **18**, 5617 (1985).

[30] H. Ehrenreich and M. H. Cohen, Phys. Rev. **115**, 786 (1959).

[31] L. Wendler and T. Kraft (unpublished).

[32] L. Wendler, T. Kraft, M. Hartung, A. Berger, A. Wixforth, M. Sundadram, J. H. Englisch, and A. C. Gossard (unpublished).

[33] M. P. Stopa and S. Das Sarma, Phys. Rev. B **45**, 8526 (1992).

[34] L. Wendler, R. Haupt, and R. Pechstedt, Phys. Rev. B **43**, 14 669 (1991).

[35] L. Wendler and V. G. Grigoryan, Phys. Rev. B **49**, 14 531 (1994).

[36] L. Wendler and R. Haupt, Phys. Rev. B **52**, 9031 (1995).

[37] W. P. Chen, Y. J. Chen, and E. Burstein, Surf. Sci. **58**, 263 (1976).